

REPORT DOCUMENTATION PAGE			Form Approved OMB No. 074-0188		
Public reporting burden for this collection of information is estimated to average 1 hour per response, including g the time for reviewing instructions, searching existing data sources, gathering and maintaining the data needed, and completing and reviewing the collection of information. Send comments regarding this burden estimate or any other aspect of the collection of information, including suggestions for reducing this burden to Washington Headquarters Services, Directorate for Information Operations and Reports, 1215 Jefferson Davis Highway, Suite 1204, Arlington, VA 22202-4302, and to the Office of Management and Budget, Paperwork Reduction Project (0704-0188), Washington, DC 20503.					
1. AGENCY USE ONLY (Leave blank)		2. REPORT DATE 7 May 2007	3. REPORT TYPE AND DATE COVERED		
4. TITLE AND SUBTITLE Remote Measurement of High Temperatures in the Presence of a Strong Magnetic Field			5. FUNDING NUMBERS		
6. AUTHOR(S) Lord, Scott F.					
7. PERFORMING ORGANIZATION NAME(S) AND ADDRESS(ES)			8. PERFORMING ORGANIZATION REPORT NUMBER		
9. SPONSORING/MONITORING AGENCY NAME(S) AND ADDRESS(ES)			10. SPONSORING/MONITORING AGENCY REPORT NUMBER		
US Naval Academy Annapolis, MD 21402			Trident Scholar project report no. 355 (2007)		
11. SUPPLEMENTARY NOTES					
12a. DISTRIBUTION/AVAILABILITY STATEMENT This document has been approved for public release; its distribution is UNLIMITED.				12b. DISTRIBUTION CODE	
13. ABSTRACT The environment inside a railgun makes conventional temperature sensing techniques ineffective. Large time-varying magnetic fields induce noise into sensors with electrical connections. The high rate of change of temperature requires a fast thermal response and a fast sampling rate. Finally, the intense heat generated requires a sensor that is thermally stable over a large range of temperatures. To overcome such environmental challenges, this project utilized an interferometric technique where the temperature is measured remotely with a low power laser and a thin sapphire sensor. A sapphire sensor with a semi-reflective coating on one side and a near totally reflective coating on the other side was designed, constructed, and evaluated. To design the sensor for maximum sensitivity a computational model was developed to determine optimal coating thicknesses. To construct the sensor, nickel and nickel oxide coatings were deposited onto a sapphire dye with the use of electron-beam metal vapor deposition. A laser was directed at the sensor at normal incidence, and the reflection from the sensor was collected with a photodiode. As the sensor's temperature was manipulated between 26°C and 355°C its reflectance changed due to variations in the optical properties of the sapphire, nickel oxide, and nickel. The data indicated the sensor responded in a manner similar to the theoretical model. Based on that data, an algorithm was developed to convert the collected optical signal into temperature data, creating a functional temperature sensing system. The system was then taken to the Naval Research Laboratory in Washington D.C. where it was used to monitor the temperature of a hollowed stainless steel cylinder through which high density current pulses were forced. The optical system's performance under such conditions was compared against a type K thermocouple, and the system demonstrated superior time response and relative immunity to electromagnetically induced noise.					
14. SUBJECT TERMS interferometer, layered media, railgun, sapphire, reflectance			15. NUMBER OF PAGES 50		
			16. PRICE CODE		
17. SECURITY CLASSIFICATION OF REPORT			18. SECURITY CLASSIFICATION OF THIS PAGE	19. SECURITY CLASSIFICATION OF ABSTRACT	20. LIMITATION OF ABSTRACT

Remote Measurement of High Temperatures in the Presence of a Strong Magnetic Field

by

**Midshipman 1/C Scott F. Lord
United States Naval Academy
Annapolis, Maryland**

(signature)

Certification of Advisers Approval

**Associate Professor Samara L. Firebaugh
Electrical Engineering Department**

(signature)

(date)

**Associate Professor Andrew N. Smith
Mechanical Engineering Department**

(signature)

(date)

Acceptance for the Trident Scholar Committee

**Professor Joyce E. Shade
Deputy Director of Research & Scholarship**

(signature)

(date)

ABSTRACT

The environment inside a railgun makes conventional temperature sensing techniques ineffective. Large time-varying magnetic fields induce noise into sensors with electrical connections. The high rate of change of temperature requires a fast thermal response and a fast sampling rate. Finally, the intense heat generated requires a sensor that is thermally stable over a large range of temperatures. To overcome such environmental challenges, this project utilized an interferometric technique where the temperature is measured remotely with a low power laser and a thin sapphire sensor.

A sapphire sensor with a semi-reflective coating on one side and a near totally reflective coating on the other side was designed, constructed, and evaluated. To design the sensor for maximum sensitivity a computational model was developed to determine optimal coating thicknesses. To construct the sensor, nickel and nickel oxide coatings were deposited onto a sapphire dye with the use of electron-beam metal vapor deposition. A laser was directed at the sensor at normal incidence, and the reflection from the sensor was collected with a photodiode.

As the sensor's temperature was manipulated between 26°C and 355°C its reflectance changed due to variations in the optical properties of the sapphire, nickel oxide, and nickel. The data indicated the sensor responded in a manner similar to the theoretical model. Based on that data, an algorithm was developed to convert the collected optical signal into temperature data, creating a functional temperature sensing system.

The system was then taken to the Naval Research Laboratory in Washington D.C. where it was used to monitor the temperature of a hollowed stainless steel cylinder through which high density current pulses were forced. The optical system's performance under such conditions was compared against a type K thermocouple, and the system demonstrated superior time response and relative immunity to electromagnetically induced noise.

Keywords: interferometer, layered media, railgun, sapphire, reflectance

Acknowledgements

I would like to acknowledge the lab technicians Ken Walsh, Erich Keyes, and Charles Popp for the countless times they have helped me obtain equipment, materials or tools I needed for various aspects of this project.

I would also like to thank Dr. Montgomery for his help in learning the optical principles used in the project and for his lending of optical tools.

Lastly, my two advisors Dr. Samara Firebaugh and Dr. Andrew Smith deserve all the thanks I have to give. Whether they were showing me something as simple as how to adjust tabs in a word processing program or explaining something as complicated as setting up a finite element model for predicting temperature profiles, they always took time to answer my questions and keep me directed towards a desirable goal.

Table of Contents

ABSTRACT.....	2
Acknowledgements.....	3
Table of Contents.....	4
List of Figures.....	5
Introduction.....	6
Motivation for Project.....	6
Goals of Project.....	6
Background Research	7
Theoretical Model.....	8
Physical Principles.....	8
Calculating Reflectance	8
Calculating Changes in Physical Properties of Each Layer.....	11
Completed Model.....	12
Nickel Sensor.....	13
Sensor Design	13
Sensor Construction.....	15
Diode Laser Experimental Setup	15
Heating Block	15
Optical System.....	16
Analysis of Diode Laser Experimental Setup.....	18
Results.....	18
Optical System Modifications.....	18
He-Ne Laser Optical Setup	19
Optical System.....	19
Results.....	20
Analysis of the He-Ne Optical Setup.....	24
Noise	24
Signal Analysis	25
Proposed Sensor Modifications	25
Final Sensor	26
Sensor Construction.....	26
Optical System.....	30
Results of Final Sensor	31
Sensor Evaluation in the Presence of a Strong Magnetic Field.....	34
Setup	34
Experimental Results	36
Conclusion	39
Bibliography	41
Appendix A: Computational reflectance model	42
Appendix B: Heating block schematics.....	45
Appendix C: MatLAB algorithm to convert photodiode voltage to temperature.....	47

List of Figures

Figure 1: Illustration of interferometer operation principle.....	8
Figure 2: Illustration of layered media traveling wave definitions.....	9
Figure 3: Diagram of model attributes.....	10
Figure 4: Computational reflectance model.....	13
Figure 5: Modeled reflectance for various nickel thicknesses.....	14
Figure 6: Optimization of peak to peak reflectance.....	14
Figure 7: Initial sensor construction	15
Figure 8: Photograph of heating block and optical sensor.....	16
Figure 9: Photograph of diode laser optical system.....	16
Figure 10: Block diagram of diode laser optical system.....	17
Figure 11: Reflectance data for diode laser experiment	18
Figure 12: He-Ne laser experimental setup with acousto-optic modulator	19
Figure 13: Block diagram of He-Ne laser experimental setup	20
Figure 14: Room temperature photodiode variation.....	21
Figure 15: Heating and cooling data of the nickel sensor in the improved optical system	22
Figure 16: Temperature histories for data shown in Figure 15.....	23
Figure 17: Final sensor construction process.....	27
Figure 18: Modeled reflectance of sensor to optimize nickel oxide thickness	28
Figure 19: Optimization of peak to peak reflectance.....	29
Figure 20: Data collected for various heating evolutions of the nickel oxide sensor	31
Figure 21: Data collected for various cooling evolutions of the nickel oxide sensor.....	32
Figure 22: Result of algorithm that maps the sensor signal into a temperature plot, compared against thermocouple data.....	33
Figure 23: Portable optics table arrangement at NRL	34
Figure 24: Load frame and hollowed cylinder.....	35
Figure 25: Hollowed cylinder and faceplate assembly	36
Figure 26: Disassembled hollowed cylinder and faceplate with sensor	36
Figure 27: Current history of capacitor discharge	37
Figure 28: Sensor photodiode signal during current pulse	37
Figure 29: Magnified sensor photodiode signal resulting from pulse discharge test	38
Figure 30: Optical sensor performance compared to the thermocouple in the pulsed discharge test.....	39
Figure 31: Localized melting on end of cylinder indicates uneven current distribution	39

Introduction

Motivation for Project

This project is primarily motivated by the recent Navy effort to develop an electromagnetic railgun. An electromagnetic railgun uses electrical energy to accelerate a projectile. As such, explosive chemical propellants, which pose an explosive hazard, are not needed. Also, a railgun has the potential to accelerate the projectile faster than traditional chemical propellants given the space and weight restrictions inherent to shipboard design.

A railgun uses high density current to produce strong magnetic fields that accelerate an armature to push the desired projectile. The armature is an electrically conductive material that slides between the two rails of a railgun. A large electric potential is applied across the two rails that forces current from the high potential rail through the armature into the low potential rail. This current produces a magnetic field that accelerates the armature down the rails and out of the railgun.

As the armature slides down, the conducting rails inside a railgun heat due to electrical resistive heating and friction. So much heat is generated that the rails cannot be operated repetitiously without a thermal management system to cool the rails keeping them within their material limits. Their surfaces melt after repeated shots, altering the geometry and surface conditions for future shots. As such, thermal management is necessary to prevent uncontrolled melting. For the development of an optimal thermal management system, thermal data is desired for various locations inside the railgun environment. However, obtaining such thermal data is difficult.

Inside the railgun there are large time-varying magnetic fields during firing, which induce noise into any sensors with electrical connections. From modeling estimations by Dr. Sikhanda Satapathy and Mr. Harold Vanicek at the Institute for Advanced Technology within the University of Texas at Austin, the temperatures inside a 12m long 64MJ railgun are estimated to reach as high as 850° Celsius.¹ The current pulse occurs over a time interval of 8 ms and generates a magnetic field on the order of magnitude of 28 Teslas.² The rails inside a railgun have a very high electric potential when energized making it imperative to have robust electrical isolation schemes to prevent electrical energy from discharging through the sensing equipment. Because the technique explored in this research does not require physical connection to the sensor, the dilemmas of the magnetic field and electrical isolation are bypassed. Also, because the interferometer sensor can be made very small, it has the potential to be placed in areas an infrared camera could not capture. The small size aids rapid thermal processing due to its small thermal mass too.

Goals of Project

The goal of this research was to construct an interferometer from a sapphire wafer and correlate changes in the interferometer's optical properties to changes in temperature. In this manner, the sapphire wafer acts as a sensor for measuring temperature that does not require electrical connections. After evaluating the interferometer's optical properties at various temperatures, a

signal processing scheme was devised to display the temperature of the wafer as a function of the optical signal.

The goal for the temperature sensor was to meet the following criteria:

- Temperature range from 23° C to 900° C
- Sampling rate of at least 10 kHz
- Accuracy within +/- 15 ° C
- Relative immunity to large magnetic field interference
- Reasonable Cost

Background Research

Ernest Doebelin separates the many options for sensing temperature into five general categories in the text Measurement Systems Application and Design: thermal-expansion methods, thermoelectric sensors, electrical-resistance sensors, junction semiconductor sensors, and radiation methods.³ Because of the strong magnetic field in the railgun environment, the thermoelectric sensors, electrical-resistance sensors and junction semiconductor sensors are incompatible. These techniques require electrical leads that would be affected by the magnetic field, severely interfering with the signal they produce. Thermal expansion methods and radiation methods are left. The radiation methods are remote and avoid the interference caused by the magnetic field; however, the general means of remotely sensing temperature is through black or grey body radiation analysis. Such analysis requires analyzing the radiation emission spectrum and requires some moderate signal analysis to determine temperature. The sensors for obtaining the radiated spectrum are expensive and can not generally sample at a rate as fast as is desired for this application. This leaves the thermal expansion methods, which include bimetallic thermometers, liquid-in-glass thermometers, and pressure thermometers. The difficulty with these methods is the fast time response required. The mass of the sensor must be very small so that it can heat up to the railgun's temperature nearly instantaneously providing the desired time resolution. On the other hand, if the sensor is very small then the resulting expansion is small and difficult to measure. However, there are optical techniques capable of sensing very small changes in thermal expansion via interference patterns. Such an optical technique is the use of an interferometer. This project uses an interferometer to measure the changes in thickness and refractive index of a thin sapphire wafer.

This is not the first time an interferometer has been used to measure temperature. For example, Fabry-Perot interferometers have been used to measure temperature by Bartosz A. Grybowski *et al.* at Harvard University⁴ and V.M. Donnelly and J. A. McCaulley at AT&T Bell Laboratories.⁵ Their systems, however, were not designed for the large temperature range necessary for the rail gun application. Zhu *et al.* at the Center for Photonics Technology in Blacksburg Virginia have demonstrated a system that works over a temperature range of 230° Celsius to 1600° Celsius.⁶ However, their system used spectral analysis requiring signal acquisition of the entire visible spectrum, reducing the sampling rate to 25 Hz and making it incompatible with the desired purpose. The proposed design for measuring temperatures in the railgun is similar to such previous research except it involves a larger temperature range than most prior work and a faster sampling rate than any previously researched interferometric temperature sensor designs.

Theoretical Model

Physical Principles

The interferometer is to be constructed from a sapphire wafer by coating each side with a reflective layer. The top layer is designed to be semi-reflective, and the bottom layer is designed to be completely reflective. As illustrated in Figure 1 a coherent light source is reflected off the top layer at normal incidence. Some of the light is initially reflected by the semi-reflective surface and some passes through the layer into the sapphire. Ignoring multiple reflections for the sake of discussion, the light that passes through the semi-reflective layer reflects off the bottom layer whereupon it passes through the top layer again, rejoining the initially reflected light. Having traveled a different path length than the initially reflected light, the rejoining light has a different phase relationship and will cause interference. That interference is measured over known changes in temperature to develop a calibration curve. Once calibrated, a signal processing scheme can be devised to determine the sensor's temperature from the returned light signal and the initial temperature of the sensor.

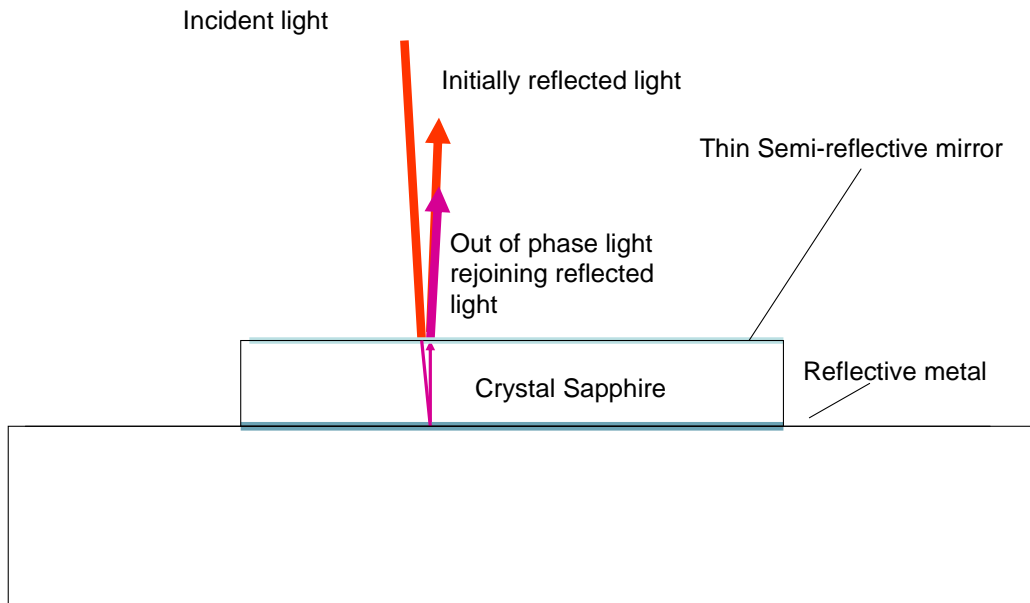


Figure 1: Illustration of interferometer operation principle

To predict the amount of interference caused by the rejoining light, one must determine the phase shift and attenuation of the light as it travels through each layer of the sensor. In order of incidence, one must determine the phase shift and attenuation from reflecting off the semi-reflective surface, the phase shift and attenuation from passing through the semi-reflective surface, the phase shift and attenuation from passing through the sapphire, the phase shift and attenuation from reflecting off the bottom reflective layer, and the phase shift and attenuation as the light travels back up through each of the layers again.

Calculating Reflectance

Because there are several layers to consider, it is practical to use matrices to model the overall reflectance of the sensor. Matrix methods are an effective means of calculating reflectance from

multilayer structures.⁷ An explanation of the mathematics used to predict the reflectance of the sensor is provided below.

Reflectance (R) is a measure of what percentage of electromagnetic power is returned off an object. It is defined as the magnitude of the square of the reflectivity. The reflectivity (r) is defined as the ratio of the incident electromagnetic wave, A_0 , to the reflected electromagnetic wave, B_0 . In equation form the reflectance and reflectivity are presented below:

$$R = |r|^2 \quad (1)$$

$$r = \left(\frac{B_0}{A_0} \right) \quad (2)$$

Where B_0 is the magnitude of the left traveling electromagnetic wave in the initial medium and A_0 is the magnitude of the right traveling wave in the initial medium as depicted in Figure 2. For the case of this experiment, the right traveling wave is the 633 nm laser light incident on the sensor, and the left traveling wave is the reflected laser light that is directed to a photodiode.

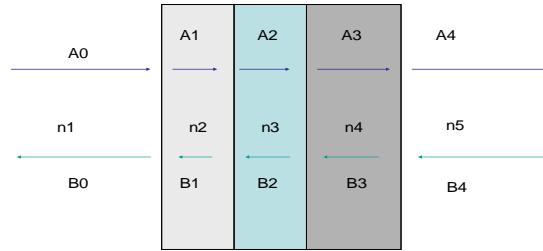


Figure 2: Illustration of layered media traveling wave definitions

The reflectivity is calculated by constructing a matrix that accounts for each layer of the object being modeled. This matrix, defined here as M , is a 2x2 matrix that is created by multiplying what are referred to as transmission matrices and propagation matrices. Transmission matrices account for the wave being incident upon an interface between two materials of differing refractive index, and the propagation matrices account for the wave propagating through a layer of specified thickness and refractive index.

The transmission matrix, defined here as D_{lk} , is used to calculate the effects of both the left traveling and the right traveling electromagnetic waves incident at the interface between the l^{th} layer and the $(l+1)^{\text{th}}$ layer. D_{lk} is mathematically defined as follows:

$$D_{lk} = D_l^{-1} D_{l+1} \quad (3)$$

Where D_l is a material property matrix that accounts for the refractive index of the l^{th} layer, n_l . D_l is defined as follows:

$$D_l = \begin{pmatrix} 1 & 1 \\ n_l & -n_l \end{pmatrix} \quad (4)$$

The propagation matrix, defined here as P_l , is used to calculate how the phase and magnitude of both the right traveling and left traveling electromagnetic waves are changed by traveling through the l^{th} layer of the sensor. P_l is defined as follows:

$$P_l = \begin{pmatrix} e^{i\phi_l} & 0 \\ 0 & e^{-i\phi_l} \end{pmatrix} \quad (5)$$

Where ϕ_l depends on the layer's thickness (d_l), refractive index (n_l), and the wavelength (λ) of the incident light. ϕ_l is defined as follows:

$$\phi_l = \frac{2 \pi d_l n_l}{\lambda} \quad (6)$$

The M matrix is constructed by multiplying the transmission matrix and propagation matrix for the layers in the order the light is incident upon each respective layer. For this project there are 5 layers: air, the top semi-reflective film, the sapphire, the bottom reflective film, and air again as illustrated in Figure 3. Because the bottom reflective layer is so thick, virtually no light passes through it into the 5th layer of air and no light propagates back through it into the sapphire.

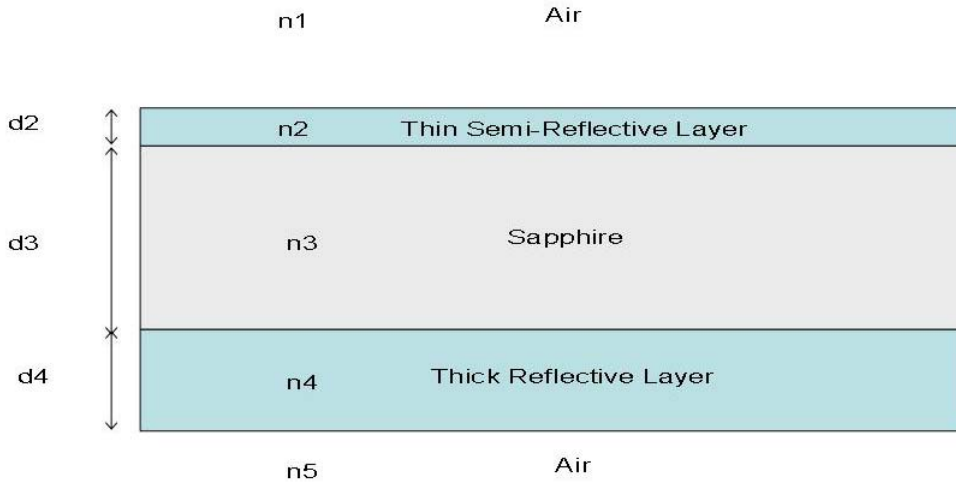


Figure 3: Diagram of model attributes

With the five layers shown above M is mathematically defined as follows:

$$\begin{pmatrix} M_{11} & M_{12} \\ M_{21} & M_{22} \end{pmatrix} = D_{12} P_2 D_{23} P_3 D_{34} P_4 D_{45} \quad (7)$$

Where the subscripts of M indicate the row and column of the elements of the M matrix, the subscripts of D represent the layer numbers creating an interface, and the subscript of P represents the layer number through which electromagnetic waves are propagating. It is assumed there are no appreciable effects on the electromagnetic waves as they travel through the air from the laser to the sensor nor as they travel through the air from the sensor to the photodiode. As such, there are no P_1 and P_5 matrices because they would represent changes caused by the laser traveling through the air to reach the sensor and the photodiode.

With the M matrix calculated one can determine the magnitude of the left traveling and right traveling electromagnetic waves in any layer via the following relationship.

$$\begin{pmatrix} A_0 \\ B_0 \end{pmatrix} = \begin{pmatrix} M_{11} & M_{12} \\ M_{21} & M_{22} \end{pmatrix} \begin{pmatrix} A_l \\ B_l \end{pmatrix} \quad (8)$$

Where A_l is the magnitude of the right traveling wave in the l^{th} layer, and B_l is the magnitude of the left traveling wave in the l^{th} layer. Using Equations 1, 2 and 8, the reflectance (R) of the sensor simplifies to the following.ⁱ

$$R = |r|^2 = \left| \frac{M_{21}}{M_{11}} \right|^2 \quad (9)$$

Note that normal incidence is assumed throughout this derivation, and the equations listed above are simplified accordingly.

Calculating Changes in Physical Properties of Each Layer

Equations 5 and 6 demonstrate that the propagation matrix depends on the thickness and index of refraction of each layer. So, the reflectance of the sensor changes with temperature because the optical properties of the material in each layer change with temperature. The change in the thickness, d_l , and index of refraction, n_l , of the l^{th} layer can be calculated using the following relationships:

$$n_l = \frac{1}{\alpha} \frac{dn_l}{dT} \quad (10)$$

ⁱ Pochi Yeh provides a thorough proof of the matrix method employed to determine the reflectance of the sensor in the text, Optical Waves in Layered Media.

$$d_i = \frac{1}{\beta} \left(\frac{d}{dT} (d_i) \right) \quad (11)$$

Where α is the temperature coefficient of refractive index, β is the temperature coefficient of thermal expansion, n_i is the index of refraction, and d_i is the thickness.⁵

Over a large temperature range α and β are not constant. As such, the most accurate means to predict the thickness and index of refraction for each layer is using previously constructed polynomial fits provided by other research. The percent change in thickness of the sapphire for a given change in temperature is provided by Touloukian and Kirby in their text Thermophysical Properties of Matter.⁸ The percent change in thickness calculated from 293 K to 1900 K is as follows:

$$\Delta L / L_0 = -0.192 + 5.927 \times 10^{-4} T + 2.142 \times 10^{-7} T^2 - 2.207 \times 10^{-11} T^3 \quad (12)$$

Where $\Delta L / L_0$ is the percent change in thickness and T is the temperature in Kelvin.

The index of refraction of sapphire as a function of temperature between 24 ° and 1060 ° C is provided by Tapping and Reilly as the following:

$$n_s(T)_{633nm} = 1.76565 + 1.258 \times 10^{-5} T + 4.06 \times 10^{-9} T^2 \quad (13)$$

Where $n_s(T)_{633nm}$ is the index of refraction of sapphire for light with a wavelength of 633 nm and T is the temperature in Celsius.⁹

The index of refraction used for nickel was $1.9712 - 3.724 \times j$.

Completed Model

Using the previously described polynomial fits and theoretical modeling techniques a program was constructed in MATLAB[®] to calculate the reflectance of the sensor with different material combinations at various temperatures. See appendix A for the program code. Figure 4 illustrates an example of the results of the model for a top semi-reflective nickel layer of 5 nm.

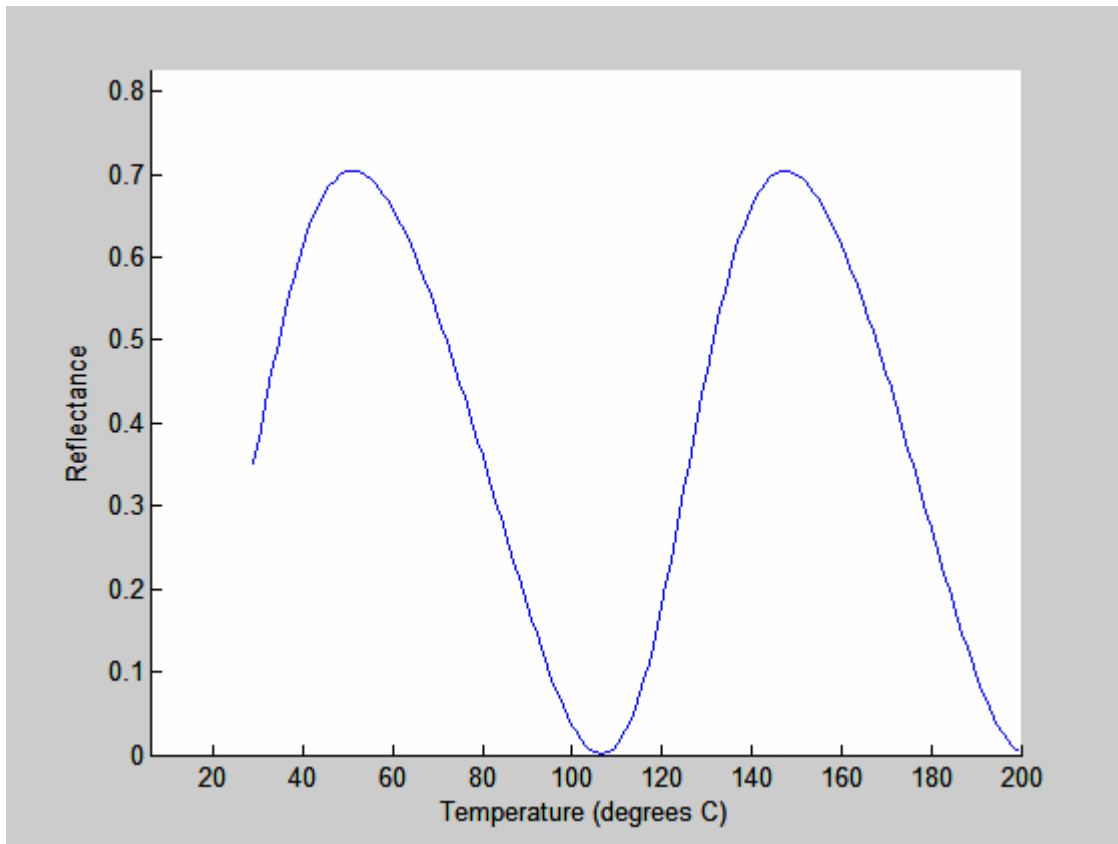


Figure 4: Computational reflectance model

Nickel Sensor

Sensor Design

To determine the optimal semi-reflective layer thickness, the reflectance model was iterated with various thicknesses for the top semi-reflective layer of nickel. The room temperature sapphire thickness was considered fixed because the dyes were pre-cut from the vendor. Also, the bottom nickel layer was considered constant because increases in its thickness had no appreciable effect on the resultant reflectance of the sensor. Figure 5 depicts the modeled reflectance of the sensor for 6 different semi-reflective nickel layer thicknesses. Figure 6 depicts the maximum peak to peak reflectance over a range of semi-reflective nickel layer thicknesses.

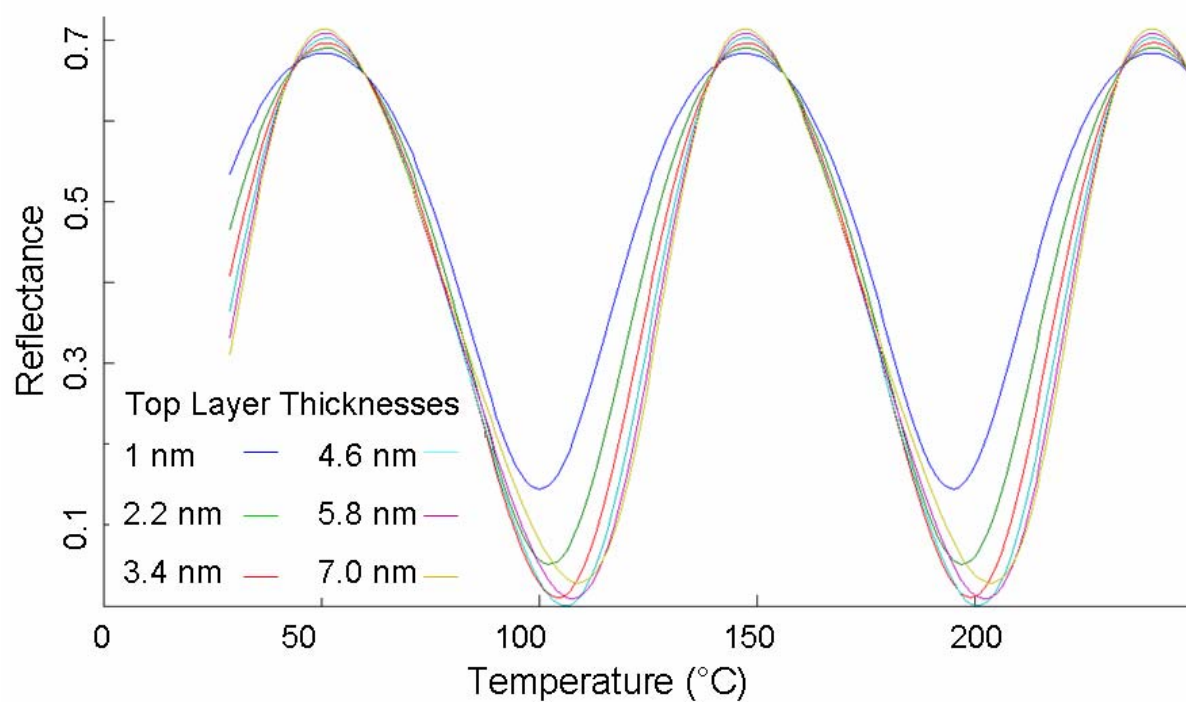


Figure 5: Modeled reflectance for various nickel thicknesses

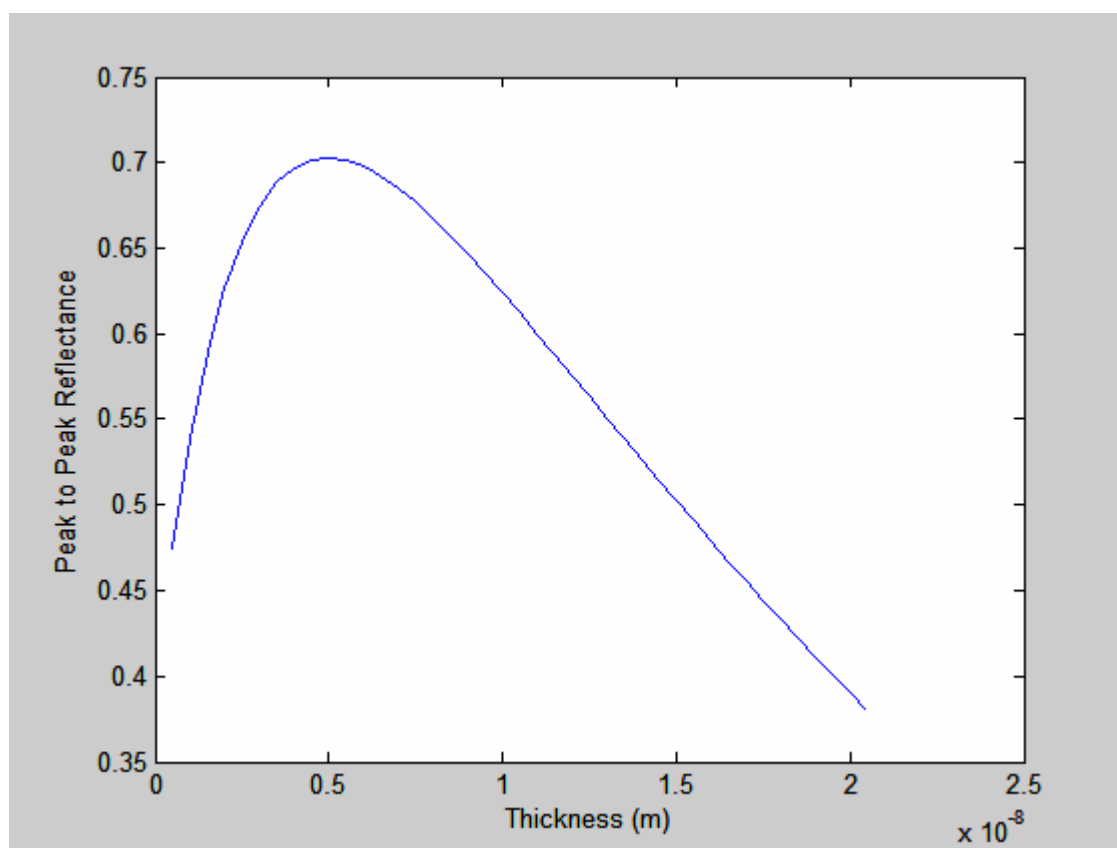


Figure 6: Optimization of peak to peak reflectance

A nickel thickness of 5.0 nm was chosen to maximize the range between minimum and maximum reflectance. By maximizing the range of reflectance values expected over a full period, the sensitivity of the sensor was maximized. Also, by making the thickness of the top layer near 5.0 nm small variations in the nickel film thickness along the surface of the sensor have minimal effects on the sensor's overall reflectance as demonstrated by the similarity of the waveforms for 3.4 nm, 4.6 nm, and 5.8 nm in Figure 5.

A new sensor was constructed further in the project to include a nickel oxide layer as the top semi-reflective layer. The computational model was altered accordingly and used again to determine the optimal nickel oxide thickness.

Sensor Construction

The sensor was constructed using a BJD 2000 E-beam Evaporation System. To construct the sensor, nickel was deposited to each side of a 1cm x 1cm x .005" thick sapphire wafer. The semi-reflective side had a nickel thickness of 5 nm, and the fully reflective surface had a nickel thickness of 80 nm. The 5 nm surface was evaporated onto the wafer via metal vapor deposition. The sapphire wafer was then removed from the evaporation system, flipped over and subsequently returned to the E-beam Evaporation System so that the 80 nm layer could be applied. The production process is illustrated in Figure 7.

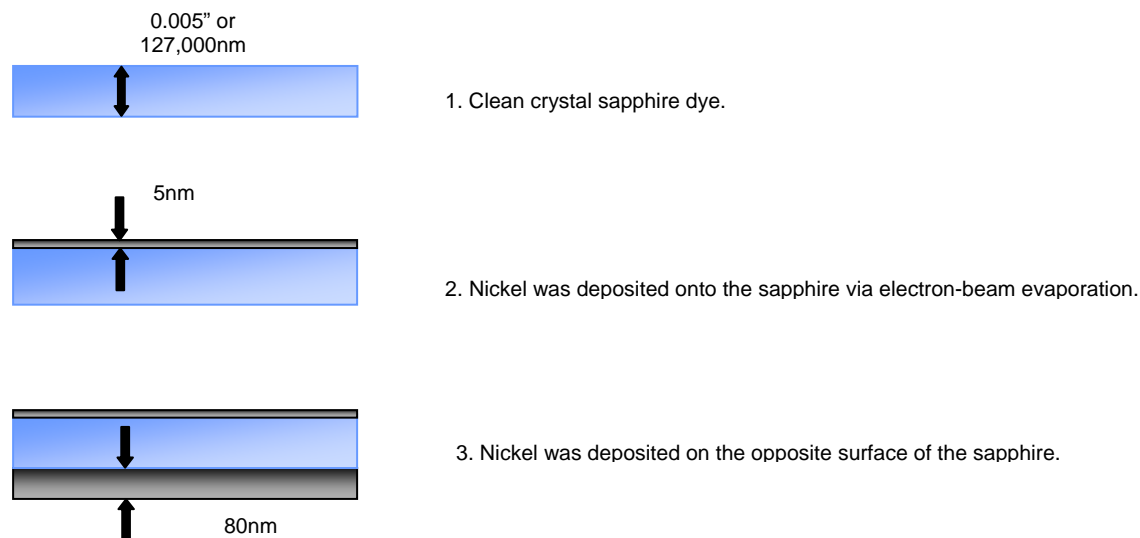


Figure 7: Initial sensor construction

Diode Laser Experimental Setup

Heating Block

A heating block to which the sapphire sensor could be clipped was crafted by the machine shop as per specifications available in Appendix B. The heating block had two heater cartridges and type K thermocouple to heat the block and measure its temperature. The thermocouple was

connected to a data acquisition multiplexer, which was connected to a computer via a National Instrument[®] digital to analog converter. Figure 8 depicts the heating block with the sensor attached.

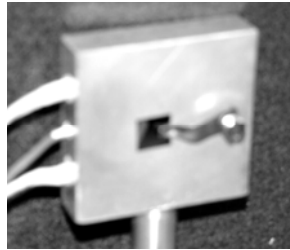


Figure 8: Photograph of heating block and optical sensor

Optical System

The heating block and sensor were placed into an optical system so that the sensor's reflectance could be measured at various temperatures. Figure 9 and Figure 10 show the optical setup.

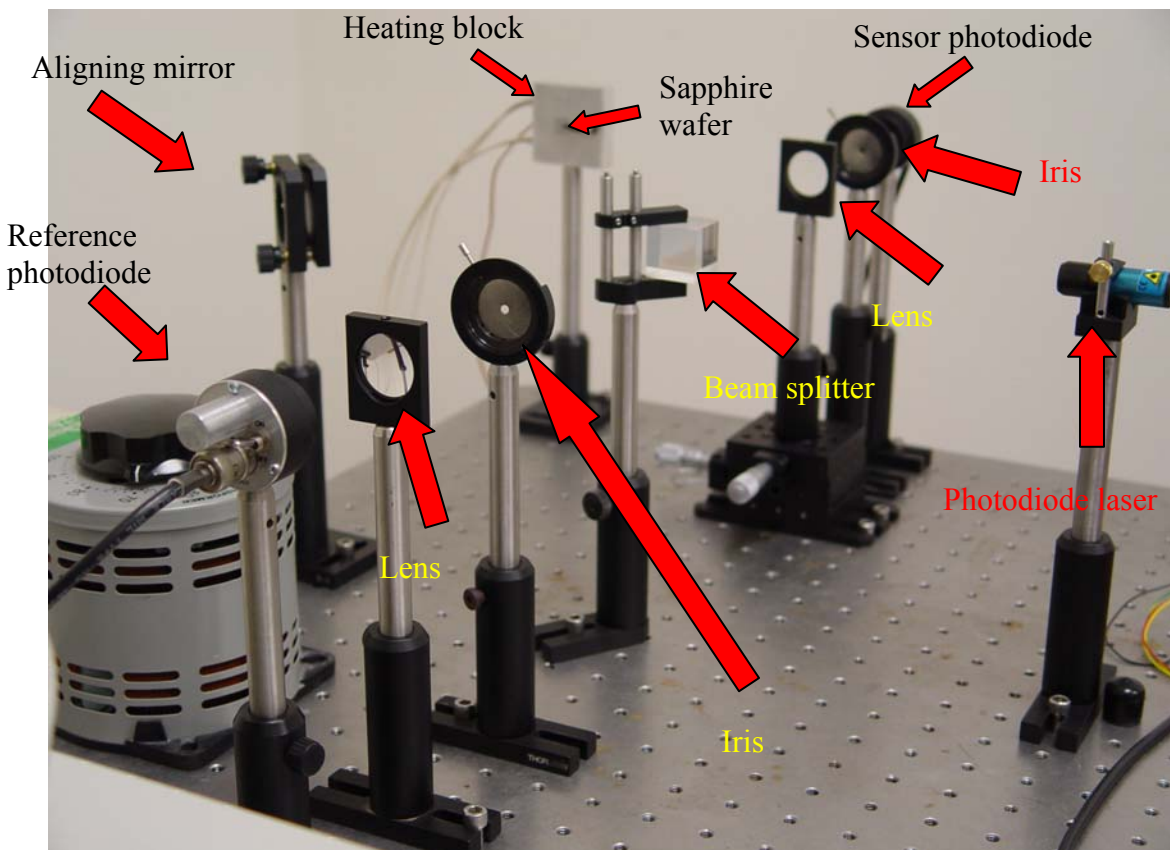


Figure 9: Photograph of diode laser optical system

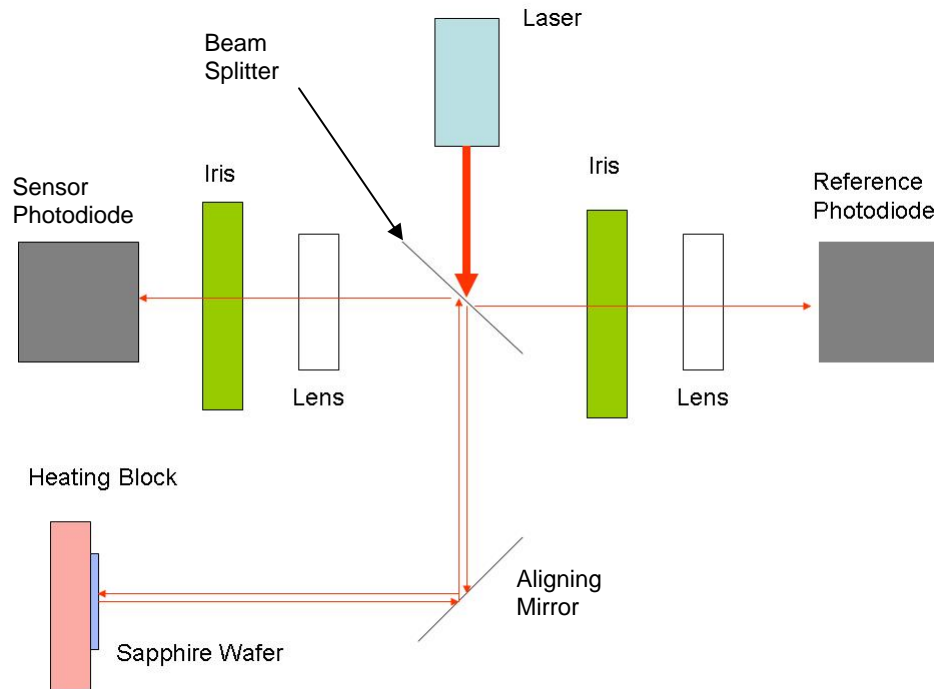


Figure 10: Block diagram of diode laser optical system

In the optical system as the light left the laser it passed through a 50/50 beam-splitter where half of the beam was diverted and focused onto a reference photodiode. The other half of the beam passed through the beam-splitter and reflected off a mirror used for aiming the laser at the wafer to ensure normal incidence. The reflected beam returned to the beam splitter where it was focused onto a second photodiode. Irises were used between each photodiode and the beam splitter to block any subsequent reflections.

The laser had an internal control that allowed the laser's power to be adjusted from an electrical signal. A 0.0 V to 1.0 V signal linearly controlled the laser's power output from minimum power (0 W) to maximum power (1 mW). The signal used to modulate the laser was a 10 kHz square wave produced by a Stanford Research Systems 3.1 MHz Synthesized Function Generator.

The modulated laser light's reflected intensity was measured via a DT-210 THOR-Labs photodiode. The photodiode signal was sent to a Perkin Elmer 7280 DSP lock-in amplifier via coaxial cable that sent the signal to a data collection computer via a GPIB bus and a National Instruments Data Acquisition Unit. The control signal sent to the laser to modulate its output power was also sent to the Perkin Elmer lock-in amplifier in order to provide a reference frequency. Effectively, the Perkin Elmer 7280 DSP lock-in amplifier filtered noise at frequencies outside a narrow band close to the reference signal's frequency. The signal collected by the reference photodiode was sent to the lock-in amplifier where it was subtracted from the photodiode signal collected from the laser light reflecting off the sensor. This provided a means to remove changes in the collected photodiode signal due to changes in the laser's power output.

Analysis of Diode Laser Experimental Setup

Results

Using the described experimental setup the data points shown in Figure 11 were collected.

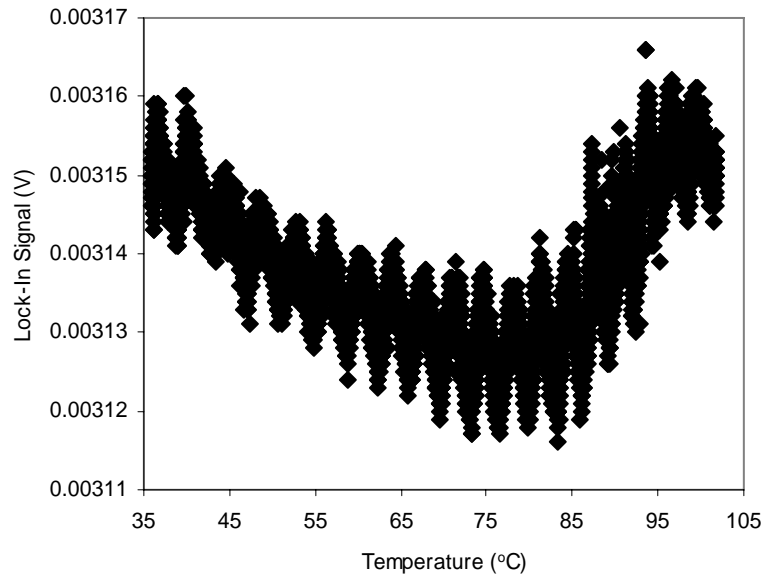


Figure 11: Reflectance data for diode laser experiment

From the data it was observed that there was substantial noise in the signal. Also, it appeared the diode laser power was oscillating.

Optical System Modifications

The diode laser power would fluctuate due to changes in the power supply and temperature of the laser cavity. While these fluctuations were partially mitigated by subtracting the reference photodiode from the sensor photodiode, the reference photodiode signal was not scaled so that its intensity matched the sensor photodiode's signal intensity. As such, fluctuations in the laser's power output were only partially removed from the final signal.

To help match the reference photodiode's signal intensity with the sensor photodiode's signal intensity, a mirror could be placed in front of the sensor and the ratio of the sensor photodiode signal to the reference photodiode signal could be measured for near 100% reflectance. That ratio could then be used to scale the reference photodiode signal so that its signal intensity matched the sensor photodiode's signal intensity. Unfortunately, the lock-in amplifier could not perform the desired scaling of a single photodiode input signal, so this technique was attempted but not employed.

As a solution, a different laser was used in the second experimental setup. A larger 35 mW He-Ne laser replaced the diode laser. The new laser had a more robust power supply and provided a more stable power output. Also, being a more powerful laser, it generated stronger signals from

the photodiodes. The major drawback of the more powerful laser was the additional safety requirements for operating a class IIIB laser. The laser's power supply had to be interlocked to the door to the laser room so that if the door opened the laser would lose power. Also, an indicating light outside the room had to be present indicating when the laser was energized. Lastly, eye protection was required when the laser was operating. The safety requirements were fulfilled and the more powerful laser was effectively put to use.

He-Ne Laser Optical Setup

Optical System

Using the more powerful laser the experiment was set up in a manner similar to the initial setup. However, the more powerful laser did not have a mechanism that allowed its power to be controlled via an electrical control signal. Thus, modulating the laser required an acousto-optic modulator (A.O.M.). An A.O.M. alternately deflects and passes the laser by passing it through a small crystal that can be mechanically oscillated by an electrical signal. For this project, the laser was modulated at 10 kHz via a control signal from the signal generator used in the initial experimental setup.

After the light passed through the A.O.M. the light passed through the 50/50 beam-splitter where half of the beam was diverted and focused onto the reference photodiode. The other half of the beam passed through the beam-splitter and then through an iris to block the laser path when the A.O.M. was in its deflecting state. After passing through the iris the light reflected off a mirror used for aiming the laser at the wafer to ensure normal incidence. The laser reflected off the sensor and returned to the beam splitter where it was focused onto a second photodiode. Irises were used between each photodiode and the beam splitter to block subsequent reflections. Figure 12 and Figure 13 depict the new optical setup.

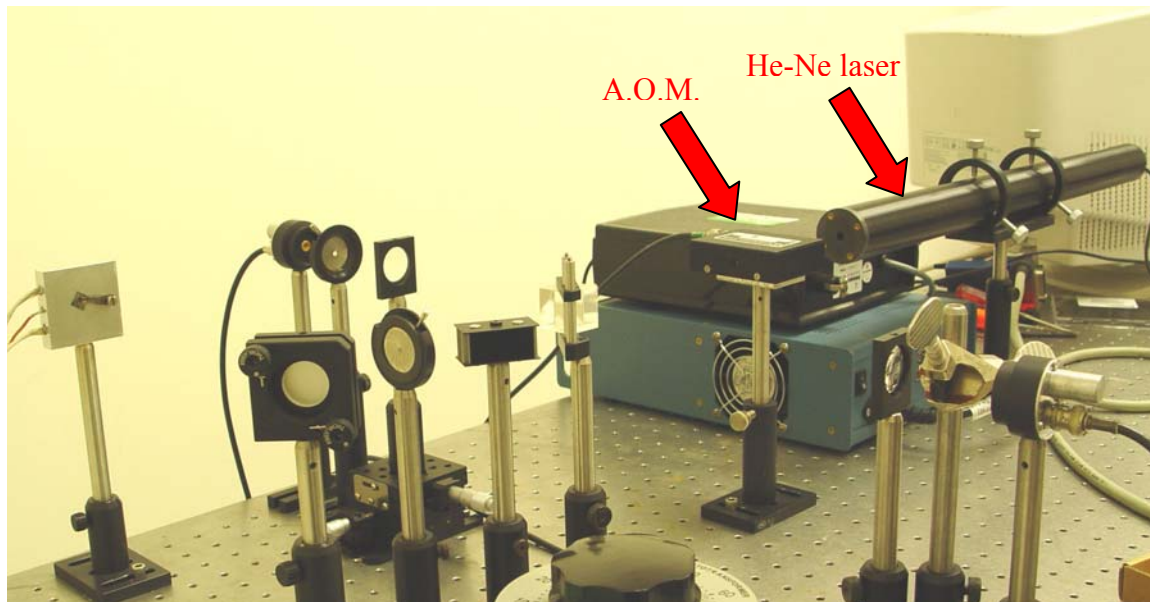


Figure 12: He-Ne laser experimental setup with acousto-optic modulator

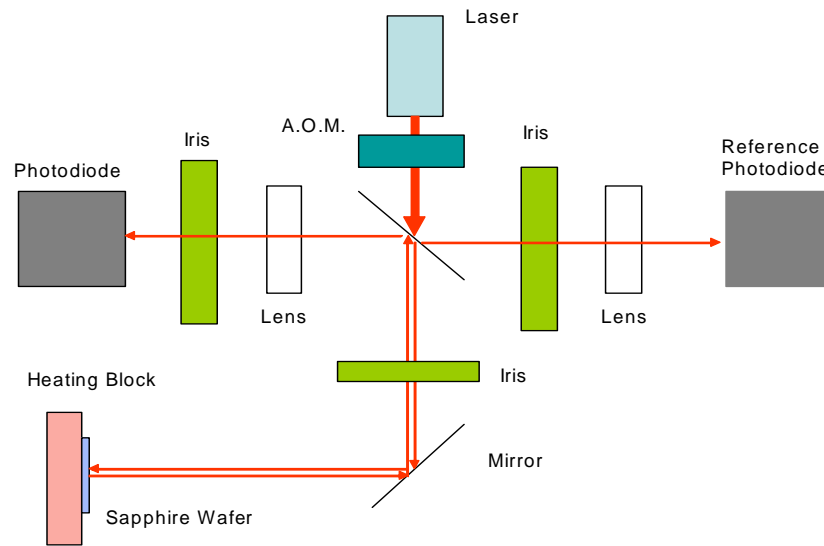


Figure 13: Block diagram of He-Ne laser experimental setup

Results

The range of voltages collected by the photodiode from the experimental set up at room temperature were observed and recorded over a 20 hour period to establish a baseline voltage shown in Figure 14. Temperature data were recorded from a thermocouple over this period, and it was determined that room temperature stayed between 28.0°C and 30.0°C for the entire time interval. From the data a baseline laser intensity of 1.4 mV was determined; however, it was observed that the setup generated a photodiode voltage between 1.1 mV and 1.8 mV. With such a large range in signal intensity some concern existed that the signal would be affected by noise from the changes in laser power.

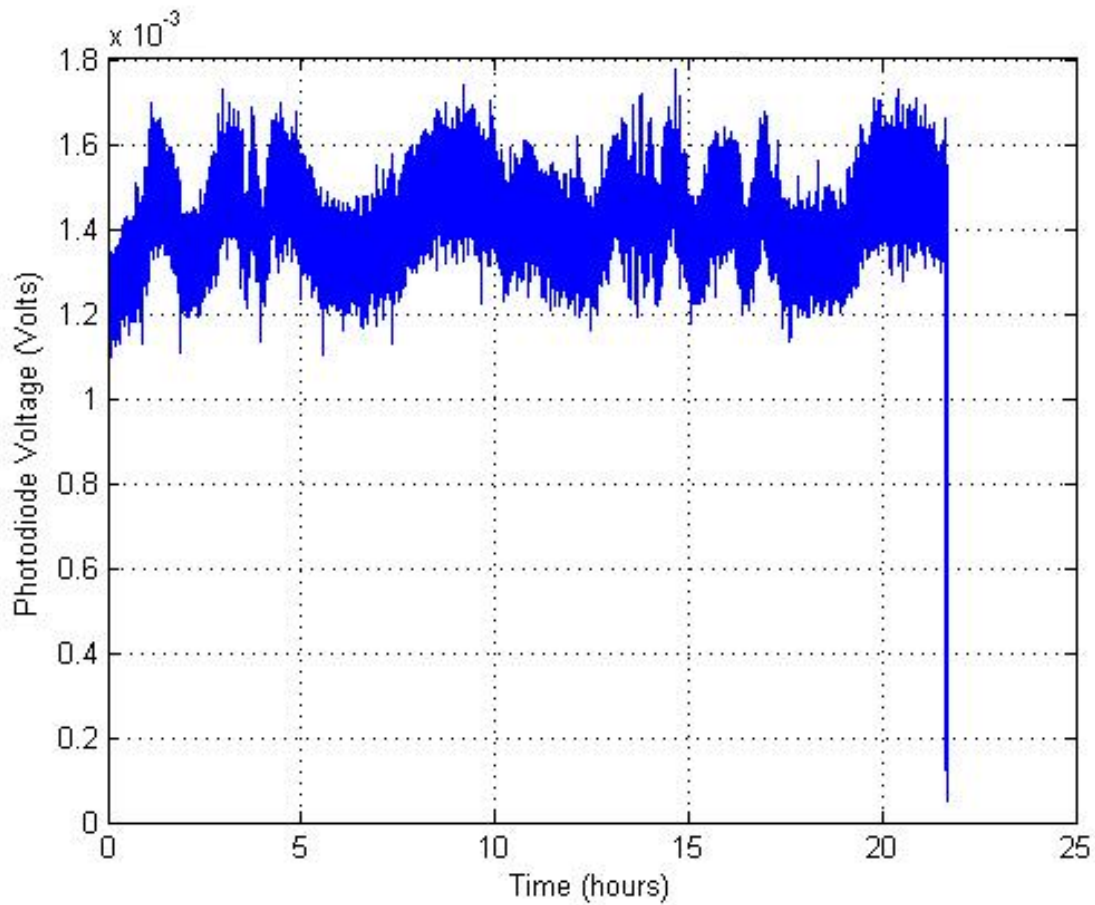


Figure 14: Room temperature photodiode variation

At the end of the data collection shown in Figure 14 one notices a drop in the signal. This is caused by the interlock that turns the laser off when the door is opened. When the laser room was entered after the 22 hour period the laser turned off and the drop in laser power was recorded before data recording was discontinued.

After the baseline collection, several heating and cooling cycles were repeated to record the photodiode signal at various temperatures. The results are illustrated in Figure 15.

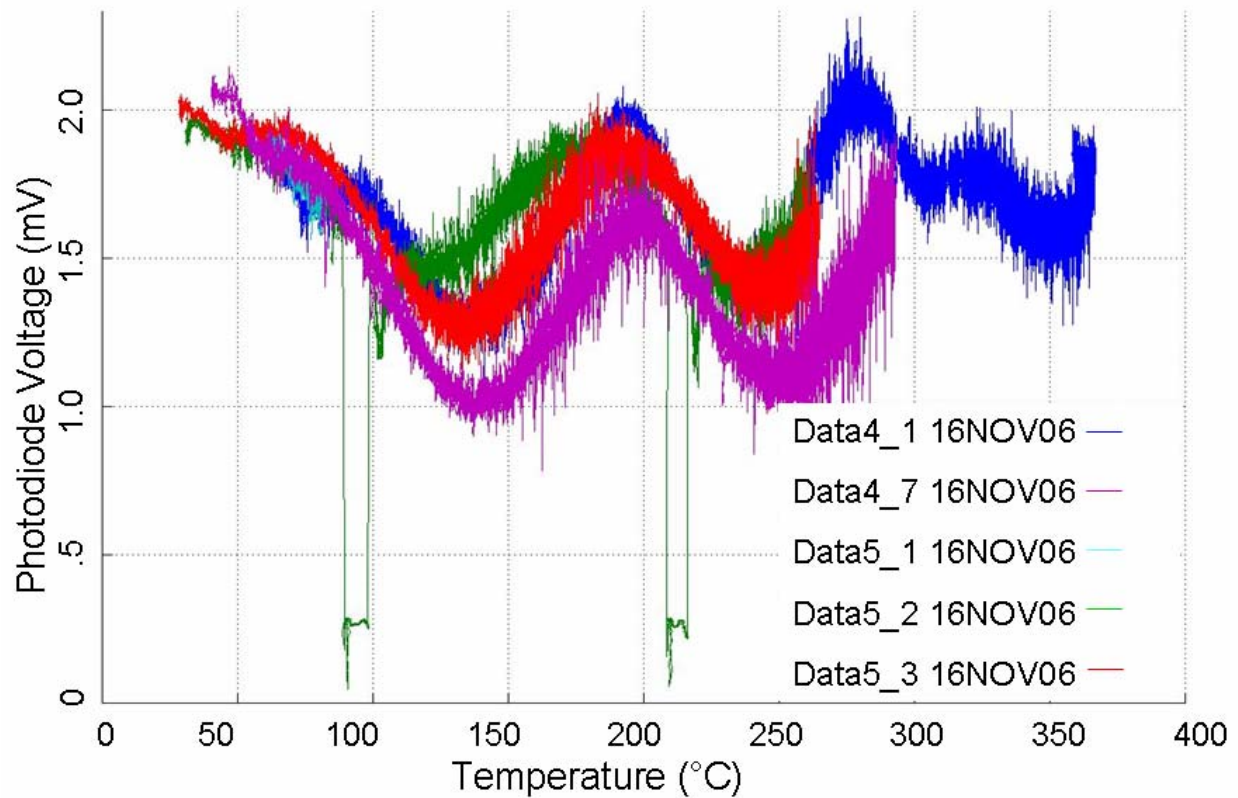


Figure 15: Heating and cooling data of the nickel sensor in the improved optical system

There are two drops in the signal of the green plot from about 90° C to 100° C and 210° to 225° C. These drops were caused by the laser turning off and subsequently turning back on due to the interlock on the laser room door.

The photodiode voltage data traces shown in Figure 15 are similar in shape to the modeled reflectance shown in Figure 5. The period for a full cycle of reflectance from the data appears to be approximately 110° C to 120° C, and in the model the period for a full cycle of reflectance is approximately 90° C to 100° C. There are several considerations to explain why the model and the data are not in perfect agreement.

The cause of the difference may be that the temperature of the sapphire sensor was not necessarily the same temperature as the thermocouple measuring the block's temperature. The thermocouple was inside the heating block closer to the heating cartridges. It took time before the thermal energy generated by the heating cartridges could reach the surface of the aluminum block. This produced a thermal gradient in the heating block that would cause the thermocouple to be a different temperature than the sapphire sensor. An option to minimize the thermal gradient between the sensor and thermocouple was to reduce the heating and cooling rate of the block.

Another effect causing the data to differ from the model was that the model assumes the air near the sensor does not change temperature as the sensor heats. However, the air did heat, altering its

refractive index and the net reflected light from the sensor. It is difficult to model this effect because the thickness and gradient of the temperature differential in the air varies with how fast the block is heated, air currents in the room, and the temperature of the sensor and block assembly.

The purpose of the model was to be an aid in designing the sensor for optimal sensitivity and to provide a general estimation of how the sensor should behave. Deviations from the model were expected, and the sensor was calibrated via signal processing of repeated data collections to account for such deviations.

The temperature history for each of the plots in Figure 15 is provided in Figure 16.

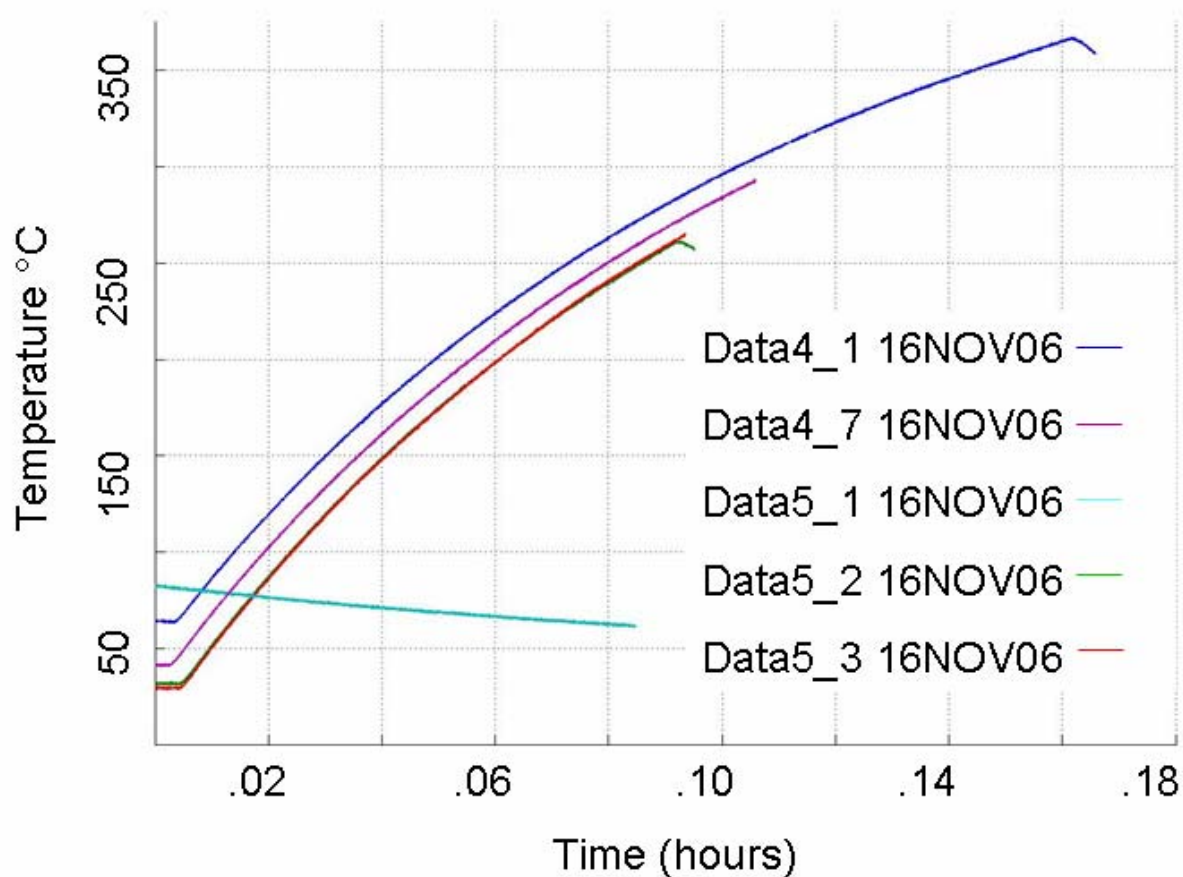


Figure 16: Temperature histories for data shown in Figure 15

Analysis of the He-Ne Optical Setup

Noise

Regarding the data shown in Figure 15, there is a significant amount of noise in the signal. One source of noise is generated by the laser being directed at the sensor at normal incidence. If perfectly normal to the sensor, part of the laser beam is reflected back into the laser cavity. This can cause a large amount of noise from interference internal to the laser. One manner to prevent this is to adjust the mirror directing the laser onto the sensor so that it is not quite normally incident and the reflection does not travel back into the laser cavity. This partially reduces the range between maxima and minima of the reflectance of the sensor as a function of temperature. Also, it causes minor deviation from the theoretical model's predictions because the model assumes normal incidence. However, in respect to reduction in range between minima and maxima and deviation from the model, the losses for slightly non-normal incidence are much smaller than the losses endured from the noise caused by the laser re-entering the laser cavity.

A second means to prevent the beam from re-entering the laser cavity is to pass the laser beam through a polarizing filter and then pass the light through a quarter-wave plate. By passing the light through the polarizing filter all light that is not of a certain polarity is blocked. When the light then passes through the quarter-wave plate, its polarization is shifted 45° . When the laser beam returns from the sensor and pass through the quarter-wave plate again, it is shifted another 45° for a total of 90° . Being shifted 90° from when it left the polarizing filter, none of the light passes back through the filter, keeping it from re-entering the laser cavity and causing interference. This method was not employed because the polarizing filter and quarter-wave plate were not available.

As a second source of noise, power fluctuations in the laser's output were still significant even with the more stable laser. One can see in Figure 14 that the laser power still fluctuated significantly compared to the signal being measured. The power fluctuated enough to change the photodiode signal between as much as 1.1 mV and 1.8 mV. From Figure 15 one can see that the data from the sensor photodiode signal usually only ranged between 1.0 mV and 2.0 mV as the sensor heated and its reflectance changed. However, the power fluctuations in the laser occurred more slowly than changes in the signal due to temperature changes during the data collection processes. As such, the expected signal is distinguishable in the collected data rather than being overwhelmed by laser power noise. Effectively, the signal is floating on the slower changing laser power baseline. Figure 15 shows that different heating cycles produced similarly shaped signals, but the data for each heating cycle appeared to be on an independent baseline voltage. In order to create more regular data, changes in laser power need to be accurately taken into account or removed.

An option available to better account for changes in laser power was to change the data collection method. Instead of having both photodiode signals sent to the lock-in amplifier and then to the computer, one could have each photodiode signal go to a data acquisition multiplexer that sends the data to an analog to digital converter card in the computer. By doing this, the data would no longer be filtered by the digital signal processes of the lock-in amplifier. The reference photodiode signal could then be scaled to be near the same magnitude of the sensor photodiode signal, and laser power could be divided out by dividing the sensor signal by the reference signal.

More importantly one could view laser power fluctuations independent of sensor reflectance changes by considering just the reference photodiode's signal. This would enable one to determine if the laser power varied significantly during the data collection. Additionally, such a setup would allow use of the smaller diode laser again. However, the more powerful He-Ne laser was not replaced as its enhanced power provided for a larger signal to be measured with the photodiodes without being so powerful that the photodiodes would saturate.

Signal Analysis

The collected data in Figure 15 and the theoretical model in Figure 5 demonstrated that a consistent periodic pattern was generated. Because it was periodic, a given voltage cannot be correlated to a given temperature without considering the starting temperature. A signal processing algorithm had to be developed to calculate the temperature from the returned photodiode voltage based on the history of the previously recorded voltages and the initial temperature of the sensor.

Proposed Sensor Modifications

Another point of consideration independent of noise was the physical integrity of the sensor. It can be seen in Figure 15 that at temperatures higher than 300° C the sensor's returned signal behaved somewhat unexpectedly. It was hypothesized that some of the nickel oxidized at that temperature changing the optical properties of the top layer and the sensor's reflectance. The top nickel layer was so thin it was difficult to visually determine if any of it oxidized as there was not a strong prismatic reflection indicative of an oxide layer. However, if the sensor was to measure temperatures up to 800° C, it was recognized that nickel alone would not be a sufficient material for the top semi-reflective layer.

As such, nickel oxide was considered as an alternative. By applying nickel and then placing the sensor in a furnace, the nickel layer could be completely oxidized. The new nickel oxide layer should remain thermally stable and not change its chemical state or optical properties between room temperature and 800° C.

The bottom reflective layer of the sensor was more difficult to replace. The bottom layer needed to allow very little transmittance to prevent light from reflecting off the surface on which the sensor would be placed and re-entering the sapphire. Such a need required the bottom layer to be relatively thick. If the bottom layer was sufficiently thick, a nickel oxide barrier could build up on the outer edge of the layer that would protect the nickel underneath it from becoming oxidized. However, the thickness of the bottom nickel layer should also be minimized to maintain the thermal mass of the sensor small and to reduce the thermal resistance between the sensor and the surface to which it is attached. A thickness of 100 nm was tested in the furnace at 800° C, and it was found that the layer completely oxidized. So, if a thick nickel layer was to be used, the nickel must be thicker than 100 nm.

Another consideration was that it may be possible to arrange the sensor so that it does not require the protective nickel oxide shell on the bottom layer. If a means could be contrived to keep the nickel on the bottom layer from being exposed to oxygen while heating it should not oxidize relieving the need for a passivating oxide layer. Because the bottom layer is between the sapphire and the object whose temperature is being measured, a thermal paste could be used between the

bottom nickel layer and the surface being measured. The paste would prevent oxygen from being able to oxidize the nickel as the sensor heated ensuring the integrity of the sensor. Additionally, perhaps just being in contact with the surface would be enough to prevent oxidation because being pressed against another surface would make it difficult for oxygen to get to the nickel layer.

A third option for the bottom layer would be to change the metal used. Gold resists oxidizing at high temperatures and may perform as an adequate substitute. However, gold does not adhere well to the sapphire, requiring an adhesion layer of chromium or titanium between the sapphire and gold. This would increase the complexity of constructing the sensor and would require the availability of gold in the metal vapor deposition system. Gold was not available during the time of this project, so this option was not attempted. Future work could be done when gold and platinum become available in the metal vapor deposition system to enhance the thermal stability and range of the sensor. Note, the reflective model constructed in MATLAB readily accommodates additional layers.

Of the proposed modifications, nickel oxide was chosen as the semi-reflective layer, and nickel was chosen for the fully reflective layer.

Final Sensor

Sensor Construction

The final sensor was constructed using a BJD 2000 E-beam Evaporation System to apply nickel to both sides of a purchased 1cm x 1cm x .005” thick sapphire wafer. The sensor had a nickel oxide layer as the top semi-reflective surface, and nickel as the bottom layer. Nickel oxide was used as the top layer because of its chemical stability when exposed to oxygen at high temperatures and its ability to act as a semi-reflective medium. Nickel was used on the bottom layer because it acted as a highly reflective mirror, had reasonable thermal conductivity, and could be pressed against the surface whose temperature was being measured protecting it from excessive oxygen when heated.

The top nickel oxide layer was created by first depositing nickel via metal vapor deposition in the E-beam Evaporation System. Then, the wafer was heated in a furnace to transform the nickel to nickel oxide (NiO). The wafer was heated to 800° C and held at that temperature for 8 hours. Using this process to transform nickel layers of similar thickness to nickel oxide was previously demonstrated by B. Sasi et al.¹⁰ The wafer was slowly cooled to ambient temperature as the furnace was turned off. The bottom nickel layer was deposited using the same metal vapor deposition process on the bottom side of the wafer after the top nickel oxide layer had been prepared. The bottom nickel layer was deposited at a thickness of 80 nm. The final sensor’s construction is illustrated in Figure 17.

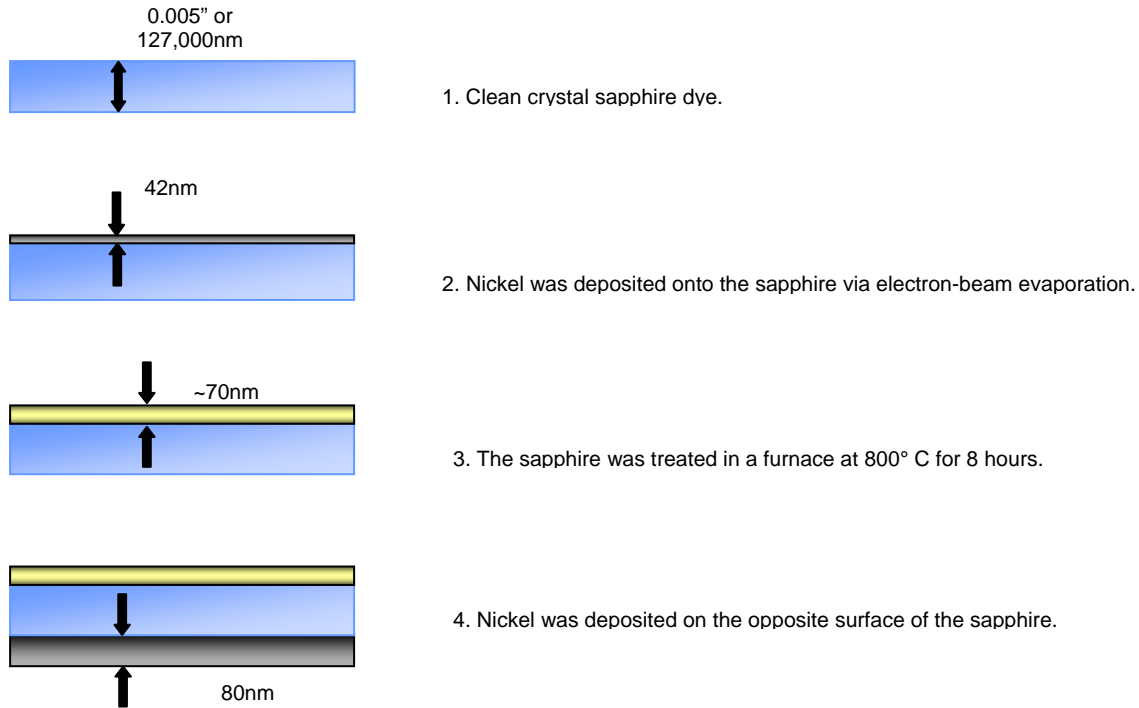


Figure 17: Final sensor construction process

The computational model described earlier was used to determine the optimal nickel oxide layer thickness. Variations in the bottom layer's thickness caused negligible changes in the modeled reflectance because the bottom layer was thick enough that it acted as a semi-infinite medium. From the model it was determined that a NiO layer of 70 nm caused the greatest peak to peak change in reflectance, resulting in the greatest sensitivity of the sensor. The nickel oxide layer can be 70 nm thick and not considered a semi-infinite medium while the nickel layer of 80 nm thickness is considered semi-infinite because nickel oxide is a transparent material while pure nickel is opaque. Figure 18 depicts the reflectance for 6 different NiO layer thicknesses and Figure 19 depicts the peak to peak reflectance for a range of NiO layer thicknesses.

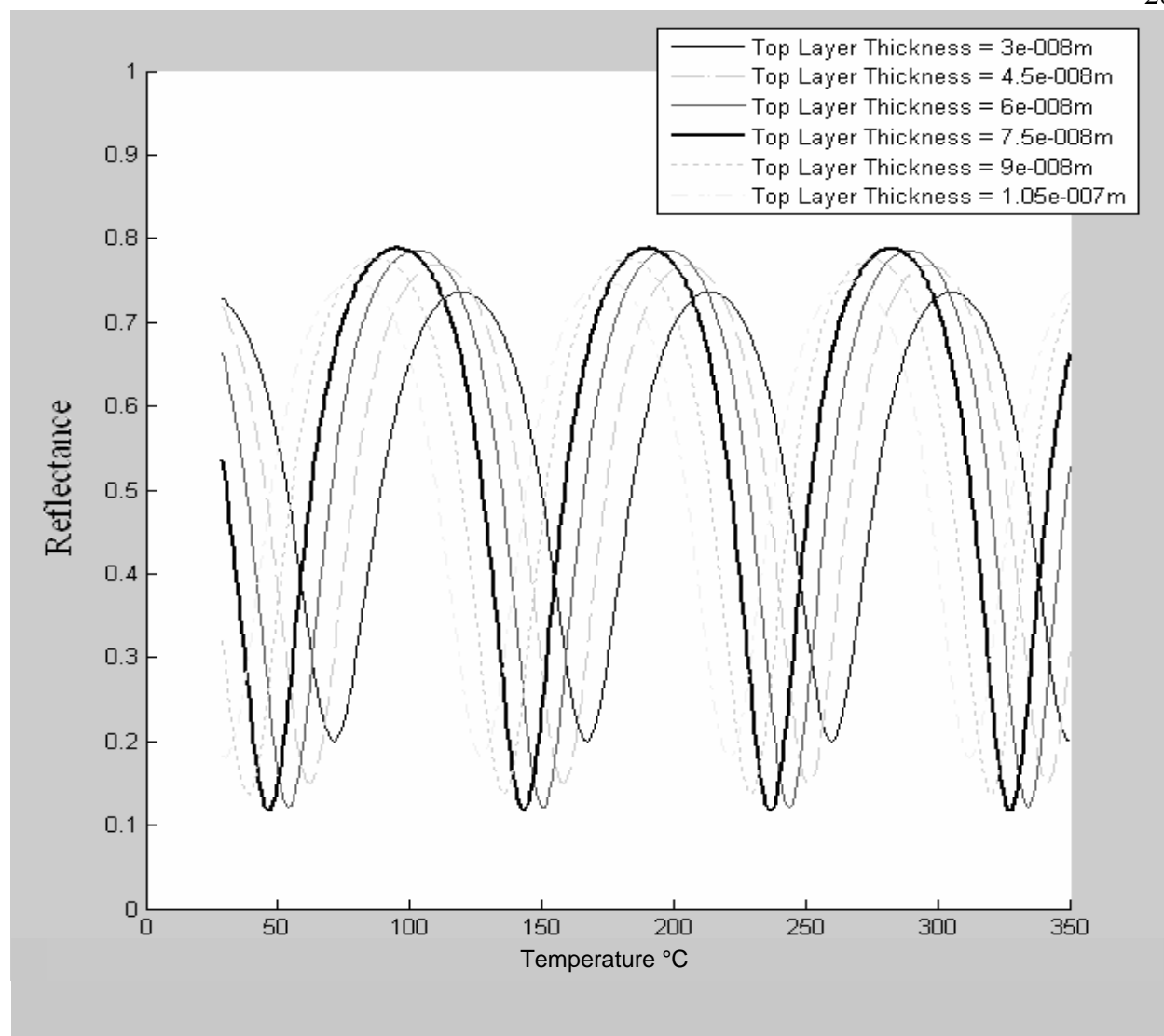


Figure 18: Modeled reflectance of sensor to optimize nickel oxide thickness

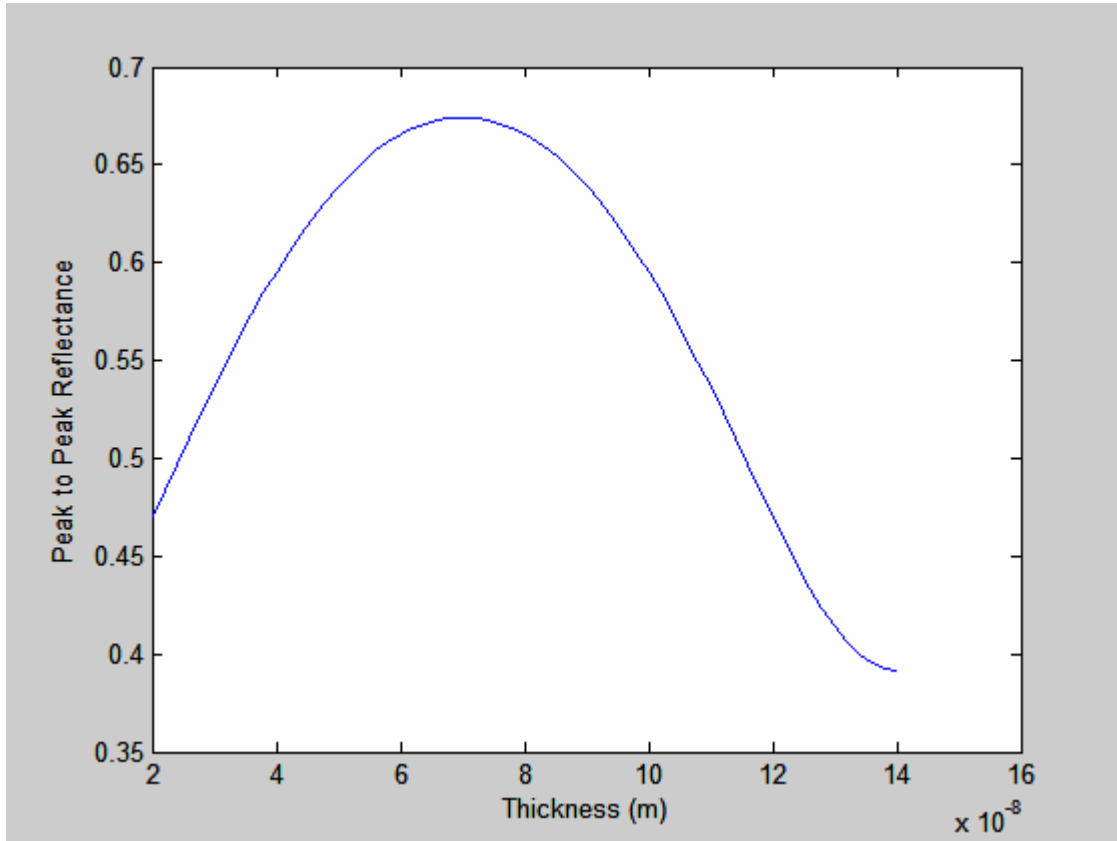


Figure 19: Optimization of peak to peak reflectance

With a goal of a 70 nm thick NiO layer on the top surface, it was necessary to calculate the amount of nickel required to produce such a thickness once oxidized. An approximation for the conversion factor was determined using equations for the volume of the layer, and the chemical reaction from Ni to NiO. Combining those equations, and assuming every nickel atom was converted to nickel oxide, and that the area remained the same, the ratio of the height of the nickel to the height of the nickel oxide was approximated by the equation below.

$$\frac{h_{NiO}}{h_{Ni}} = \frac{M_{w_{NiO}} \rho_{Ni}}{M_{w_{Ni}} \rho_{NiO}} \quad (14)$$

Where h_{NiO} is the height of the nickel oxide layer, h_{Ni} is the height of the original nickel layer, $M_{w_{NiO}}$ is the molecular weight of nickel oxide, $M_{w_{Ni}}$ is the molecular weight of nickel, ρ_{Ni} is the density of nickel, and ρ_{NiO} is the density of nickel oxide.

Table 1. Material Properties Used to Calculate Thickness Change.¹¹

$M_{w_{Ni}}$	ρ_{Ni}	$M_{w_{NiO}}$	ρ_{NiO}
58.693g/mol	8.90g/cm ³	74.692g/mol	6.72g/cm ³

Using the material values listed in Table 1, the thickness change was approximated as follows.

$$\frac{h_{NiO}}{h_{Ni}} = 1.685 \quad (15)$$

Actual thickness variations of a nickel layer being transformed into nickel oxide layer via the proposed method were measured using a Wyko optical profilometer. The results are shown in Table 2.

Table 2. Measured Layer Thickness Variation

$h_{NiO_{AVG}}$	$h_{Ni_{AVG}}$	$\frac{h_{NiO_{AVG}}}{h_{Ni_{AVG}}}$
219 nm	104 nm	2.11

The measured results produced a ratio 25% larger than the calculated ratio, which is reasonable for the assumptions of our model. The measurements made to verify the expansion ratio were done on a nickel layer thicker than the nickel layer used for the sensor. The nickel layer used for the top semi-reflective layer was 42 nm while the nickel layer measured to examine the expansion ratio was 100 nm. The resulting nickel oxide layer from the 42 nm of nickel was sufficient for the experiment in that it produced a useable signal. The thickness of the nickel oxide layer on the top of the final sensor was unable to be measured due to laboratory limitations. From the previously calculated ratio, the nickel oxide layer is estimated to be 70 nm to 89 nm.

Optical System

The final sensor was placed in two different optical systems. The first optical system was similar to the previously described configuration with the He-Ne laser, lock-in amplifier, and A.O.M. It differed in that the aiming mirror was adjusted so that the laser was not perfectly normal to the sensor and a neutral density filter was added to scale the reference photodiode's signal. The second optical system also utilized slightly off normal incidence and a neutral density filter. However, in the second configuration the lock-in amplifier and A.O.M. were removed to provide for faster sampling rates. In the second system because the lock-in amplifier and A.O.M. were removed, noise in frequencies outside a tightly controlled frequency band were not filtered out of the collected signal; however, the noise was not so significant that the signal could not be recognized.

In both systems if the laser were perfectly normal, it would return through the beam splitter back into the laser cavity, creating interference inside the laser cavity and preventing the collection of a useful signal. The aiming mirror was adjusted so that the reflected beam struck just above the hole in the laser cavity from which the laser emitted light. This shifted the laser's angle of incidence approximately 0.35° from normal incidence. Changes caused by this alteration were not recognizable in the data except for the reduction in noise from no longer having the laser interfere with itself.

The neutral density filter was added to both optical systems between the beam splitter and the reference photodiode. A neutral density filter is a device that provides a controllable means to reduce the intensity of light transmitted through it. Using the neutral density filter, the light

incident to the reference photodiode was reduced so that the signal collected by the reference photodiode was the same scale as the signal collected by the sensor photodiode. In the first system this allowed the lock-in amplifier to subtract the reference photodiode's signal from the sensor photodiode's signal, removing changes in laser power from the collected signal. In the second system, it provided a means to test the proper operation of the reference photodiode and still allowed for laser power to be subtracted from the sensor signal. For troubleshooting and configuration testing, one could adjust the neutral density filter and verify if the collected photodiode voltage changed correspondingly.

Results of Final Sensor

The newly constructed sensor was evaluated in the first improved optical configuration, and the collected data from various heating and cooling cycles is shown in Figure 20 and Figure 21. The noise in the data was approximately reduced from ± 0.25 mV to ± 0.1 mV.

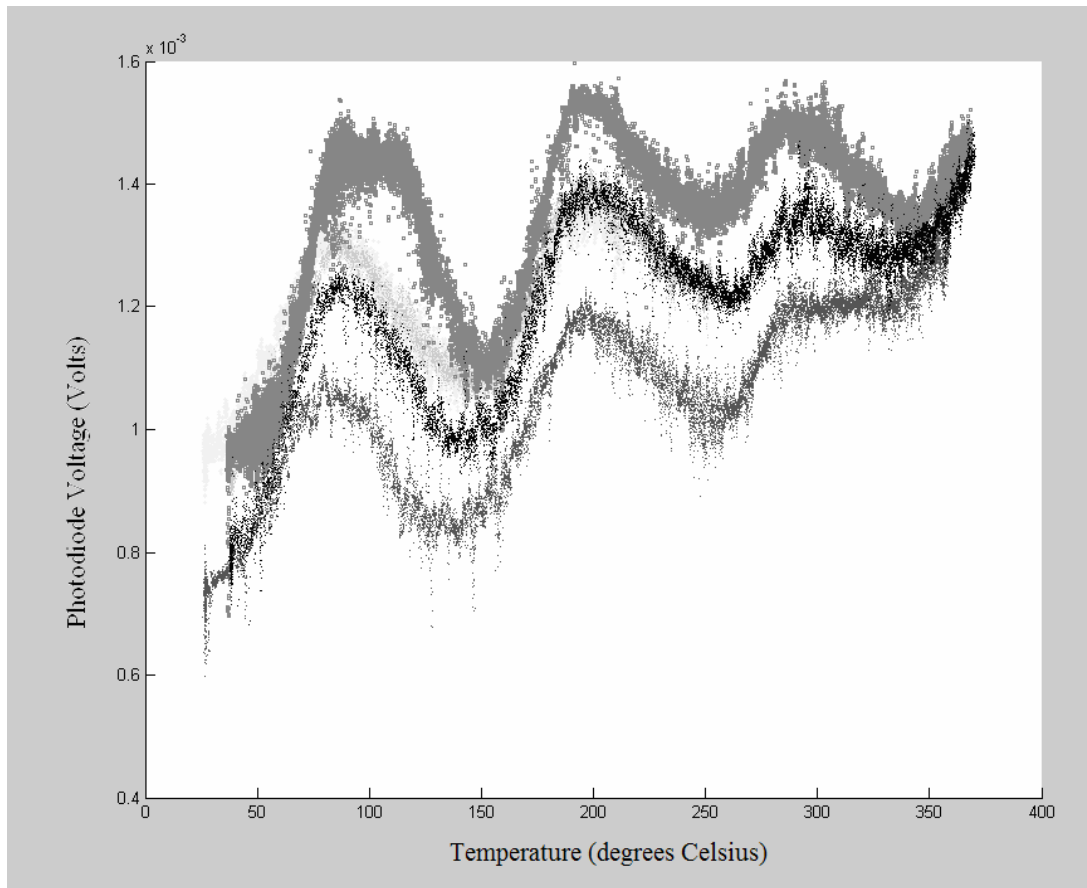


Figure 20: Data collected for various heating evolutions of the nickel oxide sensor

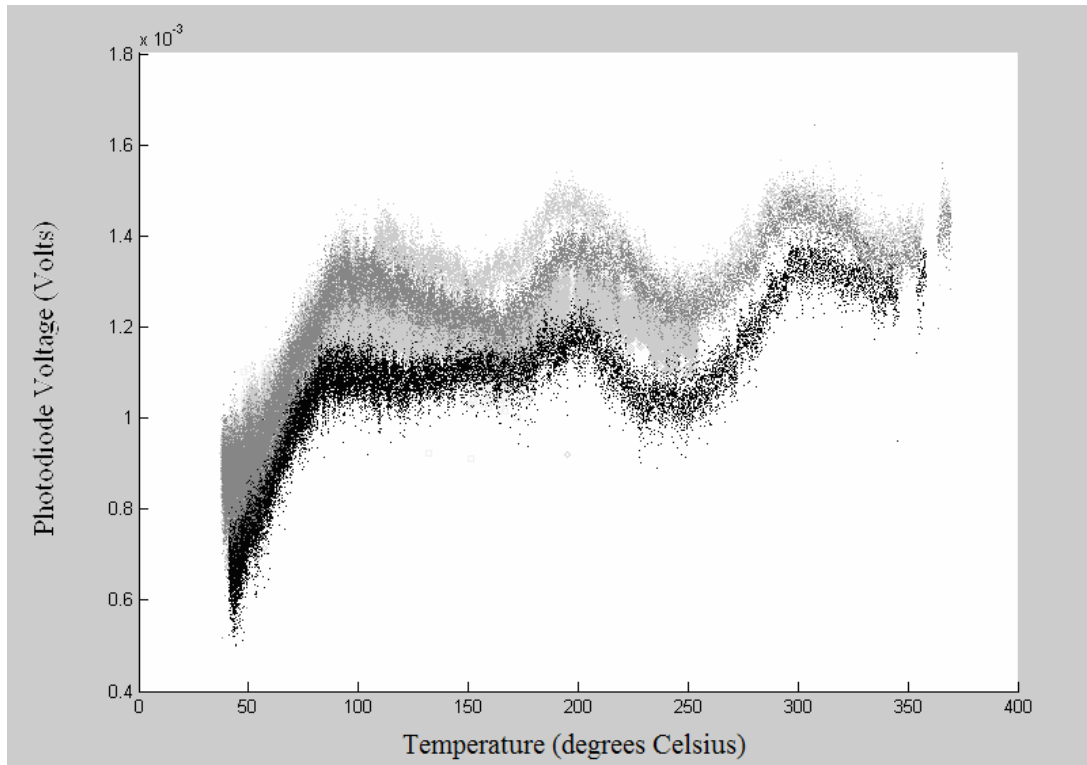


Figure 21: Data collected for various cooling evolutions of the nickel oxide sensor

It can be observed from the periodic nature of the data that relative minima and maxima always occur near specific temperatures. This phenomenon was the basis of an algorithm to be developed to calculate temperature from the photodiode signal. Also, one notices that the minima occurring near 135°C during the cool downs is less pronounced compared to the 135°C minima in the heating evolutions. It is hypothesized that differences in the temperature gradient of the air cause this dissimilarity. The sensor and heating block were cooled by removing power from the heating cartridges, letting natural convection and conduction cool the system to room temperature. This slower rate of temperature change causes the temperature distribution of the air to be different than the faster heating process. Differences in the air's temperature cause changes in the air's index of refraction. Ultimately, such changes alter the net reflectance of the sensor.

The algorithm constructed to calculate temperature is dependent on the following information: the initial temperature and the direction of the temperature change. Since the signal proceeds through the same minima and maxima regardless of direction it must be known if the sample is heating or cooling. With that information, the time of relative minima and maxima in the signal are determined and matched to corresponding temperatures. The algorithm matches minima/maxima to a temperature by assigning the next upcoming photodiode voltage minima/maxima to the next respective temperature minima/maxima depending if heating or cooling. For example, if there are minima at 45°C and 160°C and maxima at 100°C and 195°C and the initial temperature of the sensor is 27°C, as the sensor heats up the first minimum is matched to 45°C and the first maximum is matched to 100°C.

With the encountered minima and maxima correlated to temperatures, a linear interpolation was performed to calculate temperatures in between each minima/maxima. A more accurate algorithm could be developed that accounted for the curvature of the signal as it moved between peaks and troughs, but for simplicity the linear interpolation was used as the first iteration on the algorithm as it provided adequate results. Figure 22 shows the calculated results from the sensor data compared to the thermocouples collected data.

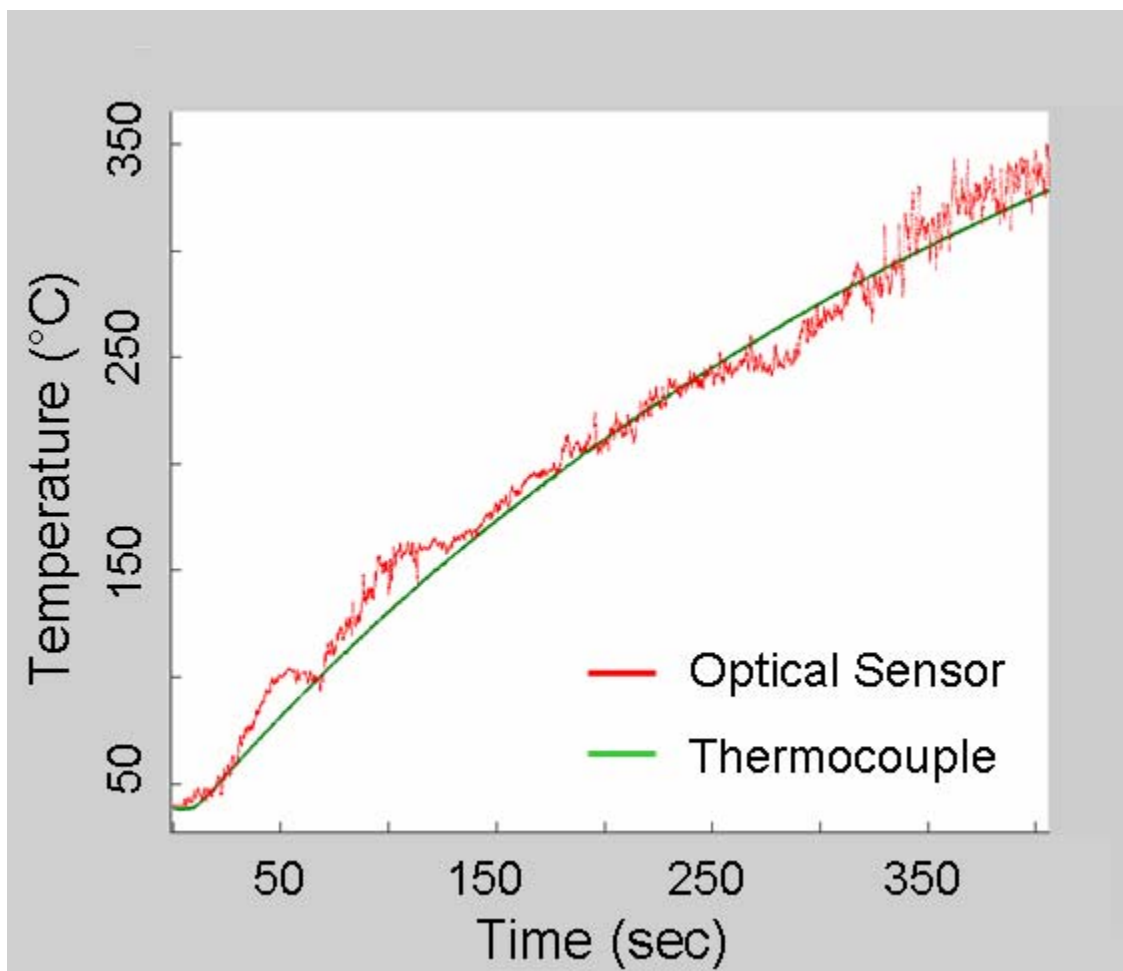


Figure 22: Result of algorithm that maps the sensor signal into a temperature plot, compared against thermocouple data

The error between the optical system and the thermocouple was an average of 8.7 °C with a standard deviation of 6.5°C. The greatest difference between the thermocouple and the optical system was measured at 35.1°C. Appendix C contains a listing of the code used to convert the photodiode signal to temperature.

The results of the 2nd optical configuration without the A.O.M. and Lock-in amplifier were similar to the 1st configuration with the He-Ne laser and the A.O.M.. However, in the 2nd optical configuration sampling occurred at 10 kHz. Sampling at 10 kHz, data could only be collected for approximately 10 seconds before the memory of the data acquisition system would require a

pause to save the data. As such, data was collected in 10 second intervals in the 2nd optical configuration.

Sensor Evaluation in the Presence of a Strong Magnetic Field

Setup

A portable optics table was taken to Naval Research Laboratory (NRL) Washington D.C. where the 2nd optical configuration was reconstructed. In the second optical configuration, the lock-in amplifier and the acousto-optic modulator were removed from the data acquisition system and optical configuration. The lock-in amplifier reduced the sampling rate of the sensor to a maximum of ~30 Hz. This new configuration allowed for sampling rates of up to 10 kHz as demonstrated at the United States Naval Academy. However, data from NRL demonstrated a 1 kHz sampling frequency was sufficient for resolving the temperature response of the sensor. The new configuration is illustrated in Figure 23.



Figure 23: Portable optics table arrangement at NRL

The sensor was placed in an electrically isolated load frame shown in Figure 24, which provided for high current density experimentation and rapid heating. The optical configuration was then aligned to measure the sensor's reflectance with the sensor secured in the load frame.



Figure 24: Load frame and hollowed cylinder

A hollowed cylinder and faceplate assembly was constructed to secure the sensor for the NRL experiment. The faceplate pressed the sensor against a flat surface cut into the hollowed cylinder providing moderate thermal contact between the sensor and cylinder and providing mechanical stability for the sensor. Additionally, thermocouples were attached to the side of the hollowed cylinder to provide temperature data before and after the current pulse. The thermocouples were electrically isolated from the data acquisition computer to prevent the current pulse from discharging through the thermocouples into the data acquisition computer. Figure 25 and Figure 26 illustrate the hollowed cylinder and faceplate assembly with the sensor inserted behind the faceplate.



Figure 25: Hollowed cylinder and faceplate assembly

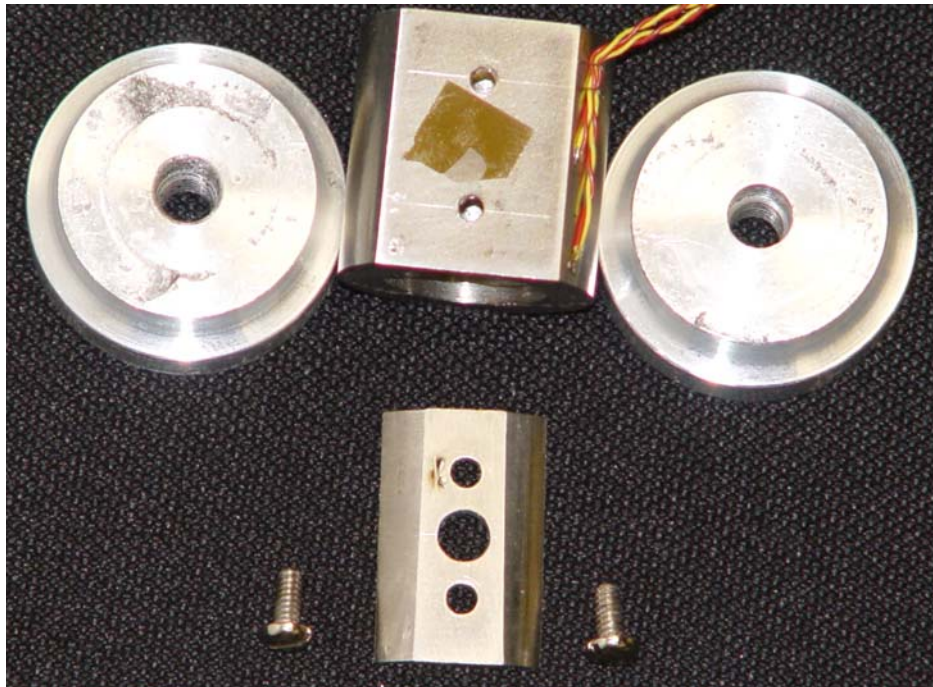


Figure 26: Disassembled hollowed cylinder and faceplate with sesnor

Once the optical configuration was aligned, the room was cleared and the capacitor banks were charged to 700 V. Upon completion of charging the capacitors, data collection was remotely started and the capacitors were manually discharged. As the capacitors discharged they forced $\sim 50,000$ A through the hollowed cylinder assembly for a 2 ms pulse.

Experimental Results

As the current was forced through the hollowed cylinder, current magnitude was recorded with a Rogowski coil. The results are illustrated in Figure 27.

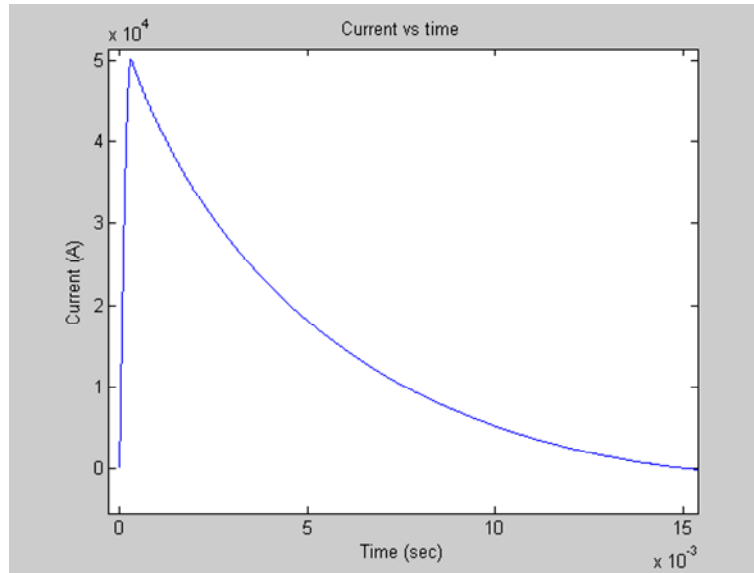


Figure 27: Current history of capacitor discharge

The sensor photodiode signal collected during the pulse is displayed in Figure 28 and Figure 29. Figure 29 shows a magnified view of the data during the first 350 ms of the pulse.

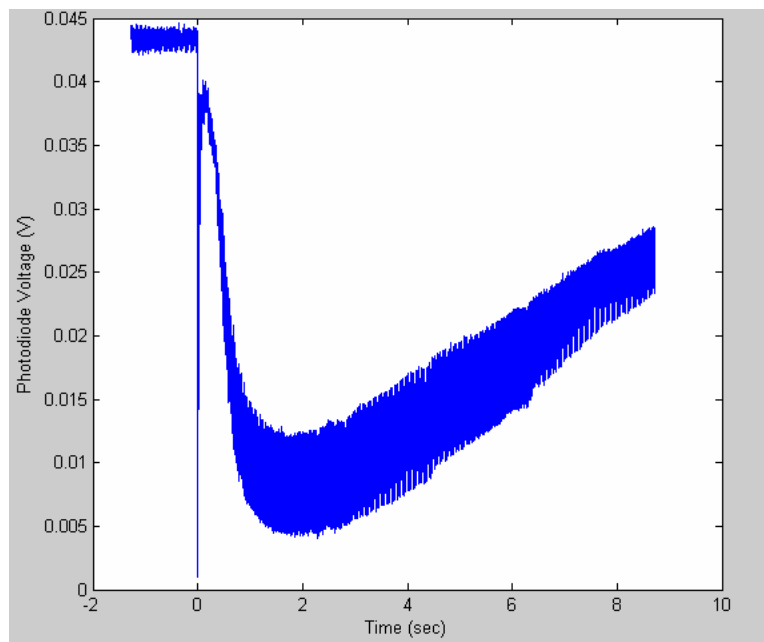


Figure 28: Sensor photodiode signal during current pulse

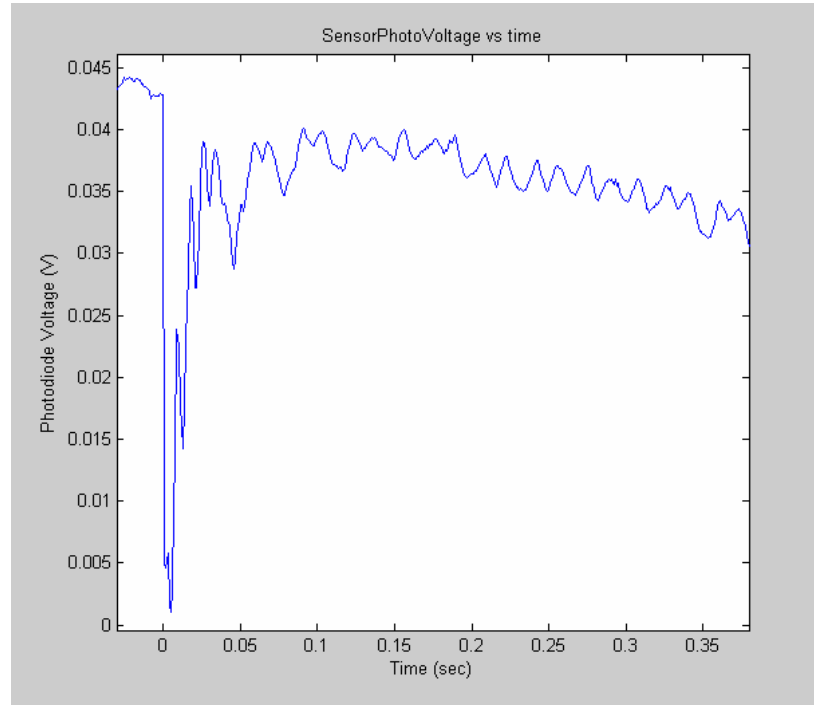


Figure 29: Magnified sensor photodiode signal resulting from pulse discharge test

In the magnified view of Figure 29, one can distinguish the initial drop in reflectance as the sensor heated up and went through a reflectance minimum near 0.01 s corresponding to 40°C. As the sensor continued to heat, the sensor's reflectance reached a maximum at ~0.03 s corresponding to 100°C and continued to heat a little longer. At approximately 0.05 seconds after the pulse started, there is a relative minimum in the collected signal. This relative minimum occurred because the sensor stops heating and starts cooling off at this time. The reflectance starts going back up as the sensor cools back down to 100°C where there is a relative maximum in sensor reflectance.

The algorithm developed to determine temperature of the sensor was applied to the photodiode signal and produced the results seen in Figure 30. Additionally, the thermocouple attached to the side of the cylinder is shown in Figure 30 for comparison to the sensor's response.

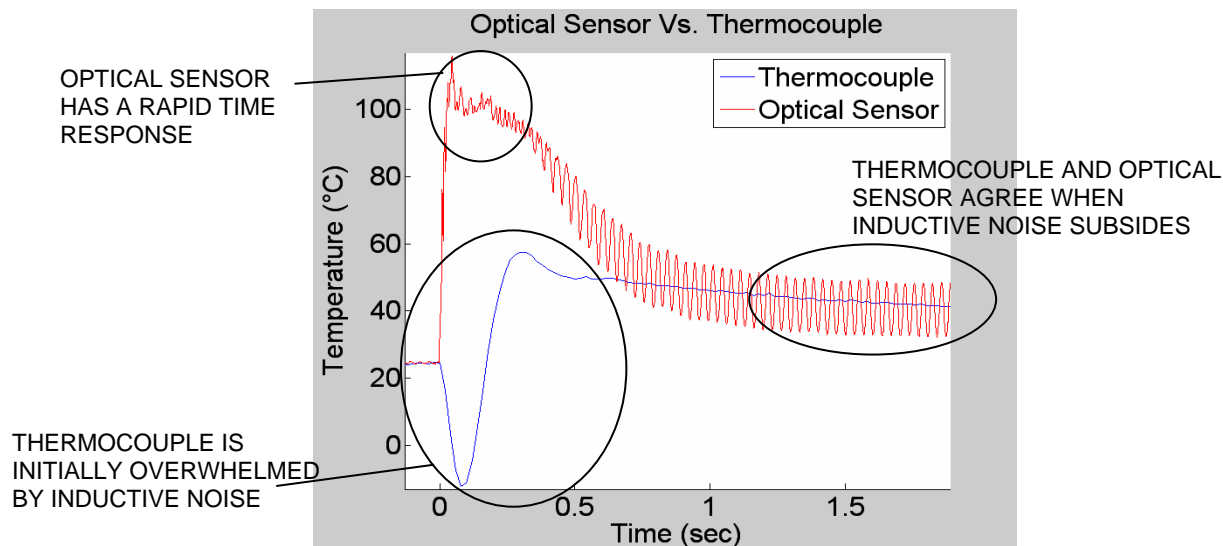


Figure 30: Optical sensor performance compared to the thermocouple in the pulsed discharge test

From the results illustrated in Figure 30 the optical sensor was relatively immune to the electromagnetically induced noise that overwhelmed the thermocouple. Also, the optical sensor had a fast time response capable of capturing a heat up rate of $\sim 2,000$ °C/sec.

There is some discrepancy between the sensor and thermocouple near 0.5 s after the pulse where it appears the thermocouple is no longer overwhelmed with inductive noise. This is most likely due to the sensor and thermocouple being different temperatures. As the current discharges through the cylinder, the current distribution is not evenly spread throughout the cylinder. As one can see in Figure 31 there are regions at the interface where the cylinder meets the load frame where melting occurs. Such melting creates paths of low electrical resistance through localized regions of the cylinder causing non-uniform heating. Such non-uniform heating could cause the sensor to heat differently than the metal where the thermocouples are attached. This effect also makes it difficult to mathematically model the temperature of cylinder as the current is forced through it.

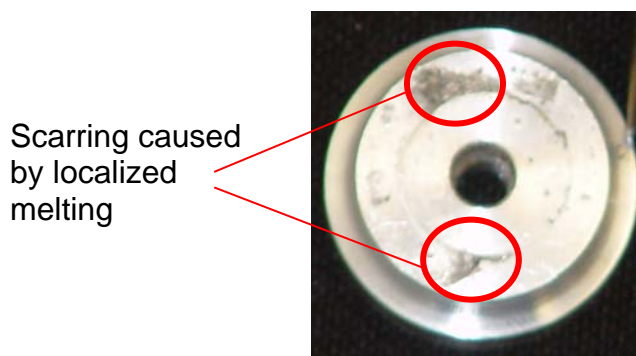


Figure 31: Localized melting on end of cylinder indicates uneven current distribution

Conclusion

A remote optical temperature sensor system with potential for operation in railgun environments was designed, constructed, and evaluated. Initially a sensor was constructed by applying nickel

coatings to the top and bottom of a sapphire dye. The thickness was determined from a parametric study of a developed computational reflectance model. The sensor was then evaluated with a 1 mW laser, and the fundamental principles of the temperature system were demonstrated. The sensor system was revised to include a 35mW He-Ne laser and an acousto-optic modulator. The He-Ne laser produced more stable power output reducing noise in the measured signal. As the sensor was tested at higher temperatures, it became apparent that the nickel did not remain thermally stable and alterations to the sensor were necessary. A sensor with a nickel oxide coating was designed and constructed, and its characteristics were evaluated with the same optical system.

An algorithm was developed to determine temperature from the sensor's returned optical signal. Those temperatures were in agreement with the response of a thermocouple in environments where electromagnetically induced noise was of negligible concern. The optical system was taken to Naval Research Laboratory where it was compared to a thermocouple in a pulsed discharge environment, imitating the environment of a railgun. The sensor demonstrated superior time response and relative immunity to electromagnetically induced noise compared to the thermocouple.

The goals for this project were to achieve a sensor with a temperature range from 23 °C to 900 °C, a sampling rate of at least 10 kHz, accuracy within +/- 15 °C, relative immunity to large magnetic field interference and reasonable cost. The final system has been demonstrated to have a temperature range of room temperature to 350 °C, sample rates of up to 10 kHz, a standard deviation of 8.5 °C, and immunity to the magnetic field interference created by the NRL pulsed discharge study. The temperature range for the device was limited in testing by experimental capability and may in fact be higher, although as discussed there may be material issues with the back Ni surface that could be solved by changing to a noble metal such as gold.

In the NRL experiments, this system far outperformed the thermocouple. The system's performance in the pulsed discharge environment shows that the optical temperature sensing system produced in this project has potential for thermal sensing in railgun studies.

Bibliography

- ¹ Dr. Sikhanda Satapathy, Harold Vanicek. Energy Partition in a Conceptual Naval Railgun at Two Scales. This work was undertaken at the Institute for Advanced Technology of The University of Texas at Austin under Contract N00178-03-D-2022 from the Naval Surface Warfare Center, Dahlgren Division. The COR is Mr. C.R. Petry.
- ² A. N. Smith, R. L. Ellis, J. S. Bernardes, and A. E. Zielinski. Thermal Management and Resistive Rail Heating of a Large-Scale Naval Electromagnetic Launcher. IEEE Transactions on Magnetics, Vol. 41, No. 1, January 2005, pg. 235-240.
- ³ Doebelin, Ernest. *Measurement Systems Application and Design*, Fifth Edition. McGraw Hill Higher Education, Singapore, 2003.
- ⁴ Bartosz A. Grybowski, Scott T. Brittain, and George M. Whitesides. Thermally actuated interferometric sensors based on thermal expansion of transparent elastomeric media. Review of Scientific Instruments, Vol. 70, No. 4, April 1999, pg. 2031-2037.
- ⁵ V. M. Donnelly and J. A. McCaulley. Infrared-laser interferometric thermometry: A nonintrusive technique for measuring semiconductor wafer temperatures. Journal of Vacuum Science Technol. A, Vol. 8, No. 1, Jan/Feb 1990, pg.84-92.
- ⁶ Yizheng Zhu, Zhengyu Huang, Fabian Shen, and Anbo Wang. Sapphire-fiber-based white light interferometric sensor for high-temperature measurements. Optics Letters, Vol. 30, No. 7, April 2005, pg. 711-713.
- ⁷ Yeh, Pochi. *Optical Waves in Layered Media*. John Wiley & Sons, Inc. United States of America, New York, 1988.
- ⁸ Touloukian and Kirby, Thermophysical Properties of Matter. The TPRC Data Series 1977, Vol. 13 pg. 176.
- ⁹ J. Tapping and M.L. Reilly. Index of refraction of sapphire between 24 and 1060°C for wavelengths of 633nm and 799nm. , J. Opt. Soc. Am. A, Vol. 3, No. 5, May 1986, pg. 610-616.
- ¹⁰ Sasi et al. Preparation of Transparent and Semiconducting NiO Films. Vacuum Surface Engineering, Vol. 68, No. 2, October 2002, pg. 149-154.
- ¹¹ Lide, David Ph.D. *CRC Handbook of Chemistry and Physics*. 82. CRC Press, New York,

Appendix A: Computational reflectance model

```
%Initializations
%*****
clear all;
close all;
InitialTemp = 29;
FinalTemp = 200;
step = 1;
lambda = 633e-9;
i = 1;
row = 1;
column = 1;

RoomTempSapphireThickness = .005*.0254; %1 inch = 0.0254 meters
dNickelTopLayerStart = 20e-9;
dNickelStep = 2e-9;
dNickelTopLayerEnd = dNickelTopLayerStart + 60*dNickelStep;
%dNickelTopLayerEnd = dNickelTopLayerStart;
dNickelBottomLayer = 80e-9;

nAir = 1;
nNickel = 1.9712-3.724*j;
nNickelOxide = 2.26;
nTopLayer = nNickelOxide;
nBottomLayer = nNickel;
%nNickel = 1.9712 + T*10^(-3)- 3.724*j - T*10^(-3)*j;

TopLayerThickness(column) = dNickelTopLayerStart;
%*****
****

for dNickelTopLayer =
dNickelTopLayerStart:dNickelStep:dNickelTopLayerEnd
    column = 1;
    TopLayerThickness(row) = dNickelTopLayer;
    for temp = InitialTemp:step:FinalTemp
        d =
dOfEachLayer(temp,RoomTempSapphireThickness,dNickelTopLayer,dNickelBottomLayer);
        dSapphire(row,column) = d(3);
        n = nOfEachLayer(temp,nBottomLayer,nAir,nTopLayer);
        nSapphire(row,column) = n(3);
        M = Mx(n, d, lambda);
        r = M(2,1)/M(1,1);
        Transmittance(row,column) = abs(1/M(1,1))^2;
        R(row, column) = abs(r)^2;
        Temperature(row,column) = temp;
        column = column + 1;
    end
    Amplitude(row) = max(R(row, :))- min(R(row, :));
    thickness(row) = dNickelTopLayer;
    row = row +1;
end
```

```

figure(1);
hold all;
x = 1;
plot(Temperature(x,[1:column-1]), R(x,[1:column-1]));
Labels = cellstr(['Top Layer Thickness = ',num2str(TopLayerThickness(x),3),'m']);
for x = 2:row-1
    plot(Temperature(x,[1:column-1]), R(x,[1:column-1]));
    Labels = [Labels; cellstr(['Top Layer Thickness = ',num2str(TopLayerThickness(x),3),'m'])];
end
xlabel('Temperature (degrees C)');
ylabel('Reflectance');
FormattedLabels = cellstr(Labels);
legend(Labels)

figure(2)
plot(thickness,Amplitude)
xlabel('Thickness (m)');
ylabel('Peak to Peak Reflectance');

%{
figure;
hold on;
for x = 1:row-1
    plot(Temperature(x,[1:column-1]), Transmittance(x,[1:column-1]))
end
%}

%{
title('Reflectance vs. Temp')
plot(Temperature, Transmittance)
title('Transmittance vs. Temp')
%}
%{
figure
plot(Temperature, dSapphire)
title('Sapphire Thickness vs. Temp')
figure
plot(Temperature, nSapphire)
title('Sapphire Refractive Index vs. Temp')
%}

function returnedMatrix = Mx(n, d, lambda)
%returnedMatrix = Mx(nArray, dArray, lambda)

D1 = Dx(n(1));
D2 = Dx(n(2));
D3 = Dx(n(3));
D4 = Dx(n(4));
D5 = Dx(n(5));

P2 = Px(phi(n(2), d(2), lambda));
P3 = Px(phi(n(3), d(3), lambda));

```

```

P4 = Px(phi(n(4), d(4), lambda));
D12 = (D1^(-1))*D2;
D23 = (D2^(-1))*D3;
D34 = (D3^(-1))*D4;
D45 = (D4^(-1))*D5;
returnedMatrix = D12*P2*D23*P3*D34*P4*D45;

function n = nOfEachLayer(T,nBottomLayer,nAir,nTopLayer)
%function n = nOfEachLayer(T,nBottomLayer,nAir,nTopLayer)
%returns n = [nAir,nNickel,nSapphire(T),nNickel,nAir];

n = [nAir,nTopLayer,nSapphire(T),nBottomLayer,nAir];

function n = nSapphire(T)
%n = nSapphire(T)
%T is temperature in Celcius
%Returns the index of refraction for sapphire for 633 nm light at a
given
%temperature

n = 1.76565 + 1.25e-5*T + 1.06e-9*T^2;

function OPL = phi(n, d, lambda)
%OPL = phi(n, d, lambda)

OPL = 2*pi*n*d/lambda;

function returnedMatrix = Px(phi)
%returnedMatrix = Dx(n)

returnedMatrix = [exp(j*phi),0;0,exp(-j*phi)];

function Newlength = lSapphire(T, l1)
%Newlength = lSapphire(T, l1)
%T is the current temp in Celcius
%l1 is original thickness of sapphire
%Function values found in Thermophysical Properties of Matter V. 13 p.
176

TK = T + 273.15;

if (TK < 293)
    Newlength = l1 + l1*(-.115 + 3.772e-4*TK - 1.999e-7*TK^2 + 8.416e-
10*TK^3)/100;
else
    Newlength = l1 + l1*(-.192 + 5.927e-4*TK + 2.142e-7*TK^2 - 2.207e-
11*TK^3)/100;
end
%}

function returnedMatrix = Dx(n)
%returnedMatrix = Dx(n)

returnedMatrix = [1,1;n,-n];

```

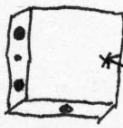
Appendix B: Heating block schematics

PREPARE ORIGINAL +1

SHOP WORK REQUEST Technical Support Department TO: Branch Head, TSD Shops		TSD JOB NUMBER		1. DATE OF REQUEST	
2. NAME OF REQUESTOR (PRINT OR TYPE)		3. DEPARTMENT		4a. PHONE EXT.	
Scott F. Lord		EEE		29 AUG 01 1-8344	
5. TITLE OF JOB		6. COURSE #		4b. EMAIL / M number	
HEATING BASE		TRIDENT		m073912 @ usm.cplc	
8. CATEGORY OF WORK		7. DESIRED COMPLETION DATE		9. FACULTY ADVISOR AND EXT.	
A. <input type="checkbox"/> COURSE SUPPORT B. <input checked="" type="checkbox"/> TRIDENT/BOWMAN PROJECT C. <input type="checkbox"/> MIDSHIPMAN PROJECT		D. <input type="checkbox"/> FACULTY RESEARCH PROJECT E. <input type="checkbox"/> GENERAL ACADEMIC SUPPORT F. <input type="checkbox"/> OTHER/ ADMINISTRATIVE SUPPORT		08 SEP 06 01 SEP 06 Prof. Firebaugh Prof. Smith	
10. URGENCY JUSTIFICATION					
11. JOB DESCRIPTION (attach drawings)					
<p>- Aluminum block</p> <p>FRONT: 2" x 2"</p> <p>TOP: 2" x .5"</p> <p>LEFT: .5" x 2"</p> <p>BACK: 2" x 2"</p> <p>BOTTOM: 2" x .5"</p> <p>RIGHT: .5" x 2"</p> <p>Drilled & tapered for 3/8" Depth: 1/4"</p> <p>Drilled diameter SNUG Depth 1.75"</p> <p>Drilled diameter .1625" Depth 1.0"</p> <p>Drilled diameter SNUG Depth 1.75"</p> <p>END PRODUCT: 3D perspective drawing of the block with dimensions and labels: 1.75", 1", 1.75", .25", SNUG FIT, Tapped for 3/8", Probe.</p>					
12. SIGNATURE OF REQUESTOR		13. SIGNATURE OF FACULTY ADVISOR (Signature indicates submittal has been reviewed for accuracy and completeness)		14. DATE	
[Signature]					
15. COMMENTS		16. ASSIGNED TO:		17. DATE ASSIGNED	
19. START DATE		20. ACTUAL LABOR HRS		21. MATERIAL COST	
				22. COMPLETED DATE	

USNA-CDA-9665/02 (Rev. Jun 2006)

PREPARE ORIGINAL +1

PROJECT WORK REQUEST Technical Support Department TO: Branch Head, Project Support Branch		TSD JOB NUMBER		1. DATE OF REQUEST <i>05 OCT 06</i>	
2. NAME OF REQUESTOR (PRINT OR TYPE) <i>Scott Lord</i>		3. DEPARTMENT		4a. PHONE EXT. <i>1-8344</i>	
				4b. EMAIL / M number <i>m073912@usna.edu</i>	
5. TITLE OF JOB <i>CIIP ATTACHMENT</i>		6. COURSE #		7. DESIRED COMPLETION DATE <i>13 OCT 06</i>	
8. CATEGORY OF WORK A. <input type="checkbox"/> COURSE SUPPORT B. <input checked="" type="checkbox"/> TRIDENT/BOWMAN PROJECT C. <input type="checkbox"/> MIDSHIPMAN PROJECT D. <input type="checkbox"/> FACULTY RESEARCH PROJECT E. <input type="checkbox"/> GENERAL ACADEMIC SUPPORT F. <input type="checkbox"/> OTHER/ ADMINISTRATIVE SUPPORT				9. FACULTY ADVISOR AND EXT. <i>FIREBAUGH 3-6715</i> <i>SMITH 3-6539</i>	
10. URGENCY JUSTIFICATION					
11. JOB DESCRIPTION (attach drawings) <i>provided piece</i>  <i>location of drilled & tapped hole</i>					
12. SIGNATURE OF REQUESTOR		13. SIGNATURE OF FACULTY ADVISOR (Signature indicates submittal has been reviewed for accuracy and completeness)		14. DATE	
15. COMMENTS		16. ASSIGNED TO:		17. DATE ASSIGNED	
				18. EST LABOR HRS	
19. START DATE		20. ACTUAL LABOR HRS		21. MATERIAL COST	
				22. COMPLETED DATE	

USNA-CDA-9665/02 (Rev. Sep 2006)

Appendix C: MatLAB algorithm to convert photodiode voltage to temperature

```

clear all
close all

LVFileName =
'N:\Trident\NRL\FiringCurrent\ActualFiringData\1323\Shot1323_07-03-
28_1313_01.lvm';
StellaFileName =
'N:\Trident\NRL\FiringCurrent\ActualFiringData\1323\1323iData.txt';
TempFileName =
'N:\Trident\NRL\FiringCurrent\ActualFiringData\1323\1323TempData.txt';

[time, RefPhotoVoltage, SensorPhotoVoltage, Temp] =
BuildFastData(LVFileName);
[Current, itime] = BuildCurrentData(StellaFileName);
[Temp, TempTime] = BuildTempData(TempFileName);

iStartTime = 0;
TempStartTime = 1.26;
SensorStartTime = 1.269;
SensorStartVoltage = mean(SensorPhotoVoltage(1:25));
StartTemp = mean(Temp(1:5));

%Align Time scales
itime = itime(:)-iStartTime;
TempTime = TempTime(:)-TempStartTime;
time = time(:)-SensorStartTime;

Tpks = [40, 100, 160, 200];
TimePkTemp = .046
VisualPkTimes = [.005, .028, .15, 1.9]

%Initializations
vpi = 1;
i = 1;
Tcalc = [];
SensorIndecies = find(time <= VisualPkTimes(vpi));
tSensorPhotoVoltage = SensorPhotoVoltage(SensorIndecies);
T2 = Tpks(i);
T0 = mean(Temp(1:5));
V2 = tSensorPhotoVoltage(end);
V0 = mean(tSensorPhotoVoltage(1:10));
Tcalc = CalculateFastTempLinear(T2,T0,V2,V0,tSensorPhotoVoltage);
i = i+1;
vpi = vpi + 1;

%Calculate temp for heat up
while VisualPkTimes(vpi) < TimePkTemp
    SensorIndecies = find(time <= VisualPkTimes(vpi) & time >
VisualPkTimes(vpi-1));
    tSensorPhotoVoltage = SensorPhotoVoltage(SensorIndecies);
    T2 = Tpks(i);
    T1 = Tpks(i-1);

```



```

        V2 = tSensorPhotoVoltage(end);
        V1 = tSensorPhotoVoltage(1);
        TcalcShort =
CalculateFastTempLinear(T2,T1,V2,V1,tSensorPhotoVoltage);
        Tcalc = [Tcalc TcalcShort];
        i = i+1;
        vpi = vpi + 1;
end

SensorIndecies = find(time <= TimePkTemp & time > VisualPkTimes(vpi-
1));
tSensorPhotoVoltage = SensorPhotoVoltage(SensorIndecies);
T2last = T2;
T1last = T1;
T2 = T2 + (T2-T1);
T1 = T2last;
V2last = V2;
V1last = V1;
V2 = V2 - (V2-V1);
V1 = V2last;
TcalcShort = CalculateFastTempLinear(T2,T1,V2,V1,tSensorPhotoVoltage);
Tcalc = [Tcalc TcalcShort];

SensorIndecies = find(time > TimePkTemp & time <= VisualPkTimes(vpi));
tSensorPhotoVoltage = SensorPhotoVoltage(SensorIndecies);
T1 = T2;
T2 = T2last;
V1 = V2;
V2 = V2last;
TcalcShort = CalculateFastTempLinear(T2,T1,V2,V1,tSensorPhotoVoltage);
Tcalc = [Tcalc TcalcShort];
vpi = vpi + 1;
i = i-1;

while VisualPkTimes(vpi-1) < VisualPkTimes(end)
    SensorIndecies = find(time <= VisualPkTimes(vpi) & time >
VisualPkTimes(vpi-1));
    tSensorPhotoVoltage = SensorPhotoVoltage(SensorIndecies);
    T2 = Tpks(i-1);
    T1 = Tpks(i);
    V2 = tSensorPhotoVoltage(end);
    V1 = tSensorPhotoVoltage(1);
    TcalcShort =
CalculateFastTempLinear(T2,T1,V2,V1,tSensorPhotoVoltage);
    Tcalc = [Tcalc TcalcShort];
    vpi = vpi + 1;
    i = i -1;
end

%Finalizations
SensorIndecies = find(time > VisualPkTimes(end));
tSensorPhotoVoltage = SensorPhotoVoltage(SensorIndecies);
T2 = StartTemp;
T1 = Tpks(1);
V2 = V0;
V1 = mean(tSensorPhotoVoltage(1:10));
TcalcShort = CalculateFastTempLinear(T2,T1,V2,V1,tSensorPhotoVoltage);

```

```
Tcalc = [Tcalc TcalcShort];
```

```
figure(1);
plot(time, SensorPhotoVoltage);
title('SensorPhotoVoltage vs time')
figure(2);
plot(itime, Current);
title('Current vs time')
figure(3);
hold all;
plot(Temptime, Temp);
plot(time,Tcalc);
title('Temperature vs time')
```

```
function [time, RefPhotoVoltage, SensorPhotoVoltage, Temp] =
BuildFastData(FileName)
%Opens the file, filters the data, and plots the data
```

```
CurrentFileName = FileName;
display(['Loading file ',CurrentFileName])
Data = dlmread(CurrentFileName, '\t');

time = Data(:,1);
SensorPhotoVoltage = Data(:,3);
RefPhotoVoltage = Data(:,2);
Temp = Data(:,4);
```

```
function [Current, itime] = BuildCurrentData(StellaFileName);
```

```
CurrentFileName = StellaFileName;
display(['Loading file ',CurrentFileName])
Data = dlmread(CurrentFileName, '\t');

itime = Data(:,1).*1e-6;
Current = Data(:,2);
```

```
function [Temp, Temptime] = BuildTempData(TempFileName);
```

```
CurrentFileName = TempFileName;
display(['Loading file ',CurrentFileName])
Data = dlmread(CurrentFileName, '\t');

Temptime = Data(:,1);
Temp = Data(:,2);
```

```
function Tcalc = CalculateFastTempLinear(T2,T1,V2,V1,V)
```

```
m = (T2 - T1)/(V2-V1);
b = (T1-V1*T2/V2)/(1-V1/V2);
```

```
Tcalc = m.*V+b;
Tcalc = Tcalc';
```